

Seventeenth Canadian Geotechnical Colloquium: The effect of cohesion loss and stress path on brittle rock strength

C. Derek Martin

Abstract: Stress–strain curves for brittle rocks show three characteristic stress levels: crack initiation, long-term strength, and peak strength. Damage-controlled testing at low confining stresses has shown that the long-term and peak strengths are sensitive to the amount of induced damage, i.e., the greater the amount of damage, the lower the long-term and peak strengths. These tests also showed that the brittle-failure process is characterized by a loss of cohesion as friction is mobilized. Excavation of a circular test tunnel in massive brittle rock resulted in failure around the tunnel. The back-calculated strength for the failed rock around the tunnel is approximately one-half of that measured in laboratory tests. Crack-induced damage of Lac du Bonnet granite, both in the laboratory and in situ, begins when the load exceeds approximately one-third of the unconfined compressive strength. However, the stress level associated with failure is a function of loading path. In the laboratory, where the loading path monotonically increases, the ultimate strength of an unconfined sample is 225 MPa. Numerical studies suggest that in situ the loading path around the tunnel is more complex, involving stress increase and decrease and stress rotation. For this loading path, failure initiates at a stress between 100 and 120 MPa. Conventional frictional failure criteria did not adequately predict the extent of brittle failure measured around the circular tunnel. The results from the damage-controlled laboratory tests and the microseismic monitoring carried out during tunnel construction indicate a constant-deviatoric-stress criterion is a reliable indicator for predicting the onset of damage. This criterion was also found to give a reasonable prediction for the maximum depth of failure around the test tunnel. The fundamental assumption in the constant-deviatoric-stress criterion is that at low confining stresses, such as those which occur around underground openings, the brittle-failure process is dominated by cohesion loss.

Key words: rock mass strength, brittle failure, cohesion loss, deviatoric stress, stress path.

Résumé : Les courbes contrainte–déformation des roches fragiles montrent trois niveaux caractéristiques de contraintes : l'initiation de fractures, la résistance à long terme et la résistance de pic. Des essais à dommage contrôlé réalisés sous de faibles contraintes de confinement a montré que les résistances à long terme et de pic sont sensibles à la quantité de dommages induits, i.e., plus la quantité de dommages est importante, plus les résistances à long terme et de pic sont faibles. Ces essais ont aussi démontré que le processus de rupture fragile est caractérisé par une perte de cohésion à mesure que le frottement est mobilisé. L'excavation d'un tunnel d'essai circulaire dans un roc massif fragile a résulté en une rupture autour du tunnel. La résistance calculée à rebours de la roche en état de rupture autour du tunnel est environ la moitié de la valeur obtenue dans les essais de laboratoire. Le dommage induit par une fissure dans le granite du Lac du Bonnet, tant dans le laboratoire que in situ, commence lorsque la charge excède approximativement un tiers de la résistance en compression non confinée. Cependant, le niveau de contrainte associé à la rupture est fonction du cheminement de la charge. En laboratoire, où le cheminement de la charge monotonique augmente, la résistance ultime d'un échantillon non confiné est de 225 MPa. Des études numériques suggèrent que le cheminement de la charge in situ autour du tunnel est plus complexe, impliquant des augmentations, des diminutions et des rotations des contraintes. Pour ce cheminement de charge, la rupture est initiée à une contrainte entre 100 et 120 MPa. Le critère conventionnel de rupture ne prédisait pas adéquatement l'importance de la rupture fragile mesurée autour du tunnel circulaire. Les résultats des essais à dommage contrôlé en laboratoire et la mesure microseismique réalisée durant la construction du tunnel indiquent qu'un critère de contrainte déviatorique constante est un indicateur fiable pour la prédiction de l'imminence de dommages. L'on a trouvé également que ce critère fournissait une prédiction raisonnable de la profondeur maximale de la rupture autour du tunnel d'essai. L'hypothèse fondamentale dans le critère à contrainte déviatorique constante est qu'à de faibles contraintes de confinement, comme celles qui se produisent autour d'ouvertures souterraines, le processus de rupture fragile est dominé par une perte de cohésion.

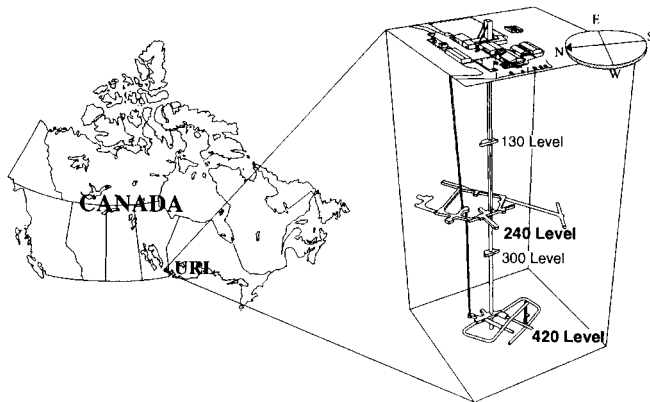
Mots clés : résistance du roc massif, rupture fragile, perte de cohésion, contrainte déviatorique constante, cheminement de contraintes.

[Traduit par la rédaction]

Received January 28, 1997. Accepted May 6, 1997.

C. D. Martin. Geomechanics Research Centre, Laurentian University, Sudbury, ON P3E 2C6, Canada.

Fig. 1. Atomic Energy of Canada Limited Underground Research Laboratory (URL), showing the two main working levels. The Mine-by Experiment was carried out on the 420 Level.



Foreword

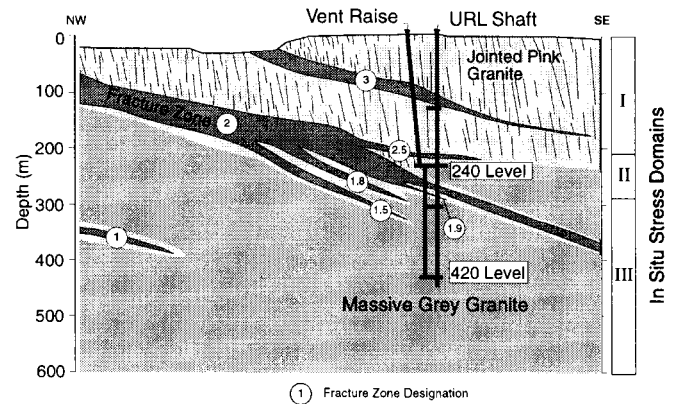
This colloquium was presented in 1993 at the Canadian Geotechnical Society (CGS) Conference in Saskatoon. At the time of the presentation, Atomic Energy of Canada Ltd. (AECL) had completed nearly two-thirds of the Mine-by Experiment project. As the colloquium draws heavily on the field results from the Mine-by Experiment, final conclusions could not be properly presented until all the results from the experiment were analyzed and reported. That task was completed in 1996 with the publication of two AECL reports by Read and Martin (1996) and Martin and Kaiser (1996). The work presented here summarizes the main findings of the author and his co-workers at AECL, in particular R. Read, on brittle rock mass failure.

Introduction

The failure process around an opening in brittle rock is often described as spalling or slabbing, and the resulting failed zone is commonly referred to as breakout, dog-ear, or V-shaped notch. Practical experience indicates that the spalling occurs in the region of maximum tangential stress around the boundary of the opening. This region is most important to the stability of an underground opening because, in extreme stress conditions, the spalling process can lead to complete collapse of the opening. This class of stress-induced failure is seldom found at shallow depths but is generally associated with deep mining operations, in rock masses typically described as sparsely fractured or massive.

Stability analyses of underground openings require an estimate of the in situ rock mass strength. In the empirical Hoek–Brown failure criterion the in situ rock mass strength is estimated by linking the rock mass rating (RMR) of Bieniawski (1979) to the Hoek–Brown empirically established constants (m , s) and the laboratory unconfined compressive strength, σ_c (Hoek and Brown 1980b). For massive rocks, RMR is typically >70 and the m and s parameters approach the values derived from intact laboratory specimens (Hoek and Brown 1988). However, practical experience indicates that even in massive brittle rock, the back-calculated strength that can be relied on around openings is usually less than 50% of the laboratory strength of intact rock (e.g., see Pelli et al. 1991; Myrvang 1991). Stacey (1981), recognizing the difficulty of estimating

Fig. 2. Northwest–southeast geological section through URL.



the strength for this class of problem, proposed a simple extensional-strain criterion based on laboratory tests of intact samples. Although application of this criterion has met with some success, it is still not obvious what fundamental mechanisms control the failure of brittle rock. The purpose of this colloquium is to investigate the brittle-failure process, both in the laboratory and in situ, and to compare the similarities and differences.

The in situ work reported in this paper, called the Mine-by Experiment, was carried out at the Underground Research Laboratory (URL) of AECL, located in southeastern Manitoba, Canada (Fig. 1). The URL is located within the Lac du Bonnet granite batholith, which is considered to be representative of many granitic intrusions of the Canadian Shield (Everitt et al. 1990). Extensive characterization of the URL revealed that jointing essentially stops at a depth of about 220 m beneath the ground surface. The Mine-by Experiment was carried out at a depth of 420 m (420 Level, Fig. 2), approximately 200 m below any regular joint patterns. Approximately 500 m of tunnel excavation at the 420 Level (see Fig. 19) encountered only six fractures, each with a trace length less than 1.5 m. Also, boreholes drilled to depths of over 1000 m in the vicinity of the URL indicate the massive granite persists with depth. Hence, one can conclude that the experiment was carried out in massive, sparsely fractured granite.

Failure in laboratory compression tests

The Lac du Bonnet granite at the 420 Level of the URL is grey in colour and generally coarsely crystalline, with 48% alkali feldspar, 17% plagioclase, 29% quartz, and 6% mica, whose mean grain sizes are 4, 4, 2, and 1 mm, respectively. The laboratory tests described in this section were carried out on samples of grey granite.

The failure of brittle rocks in laboratory cylindrical compression tests has been investigated by many researchers (e.g., see Hoek 1965; Brace et al. 1966; Bieniawski 1967; Wawersik and Brace 1971; Gramberg 1989). The testing setup used by these researchers generally followed the suggested methods now advocated by the ISRM Commission on Testing Methods (Brown 1981), i.e., the length to diameter ratio is between 2 and 3 and the diameter is greater than 54 mm (NX core). Using this configuration and with the load monotonically applied at the rate of between 0.5 and 1 MPa/s, these researchers have shown that

Fig. 3. The three parameters determined from laboratory compression test: crack initiation (σ_{ci}); initiation of sliding (σ_{cd}), and peak strength (σ_f). $\Delta V/V$, volumetric strain.

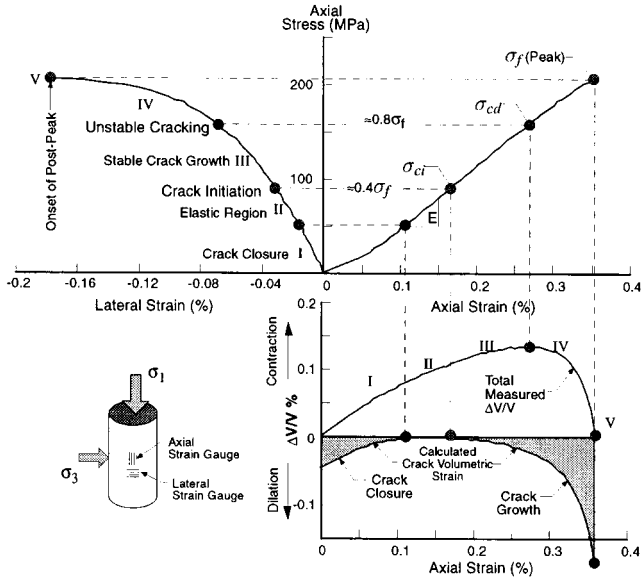
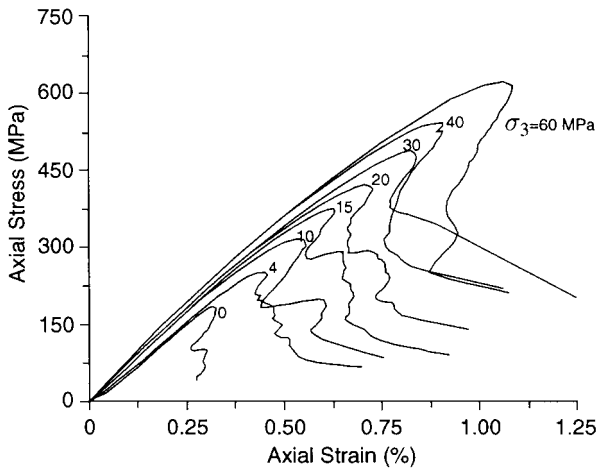


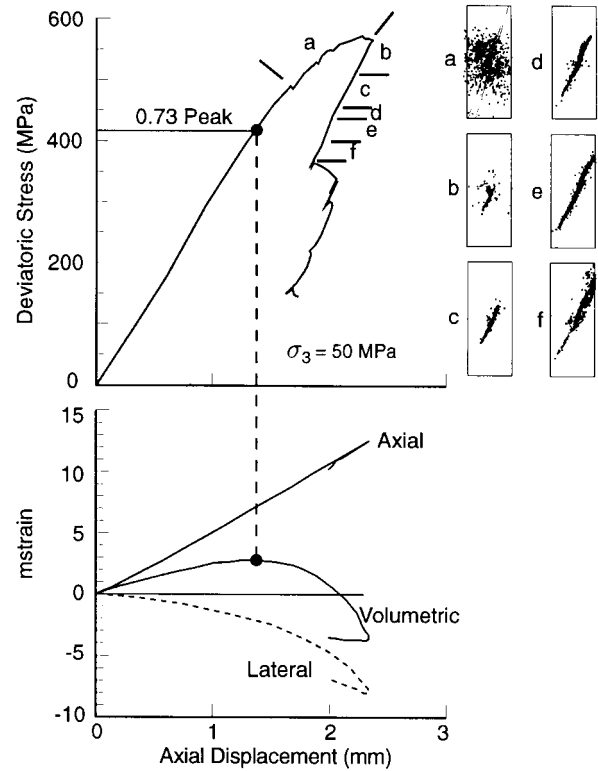
Fig. 4. Brittle failure in Lac du Bonnet granite.



the failure process is dominated by the growth of small cracks in the direction of the maximum applied load. The stress-strain curves for this test configuration display three key stress levels: (1) stress associated with the initiation (σ_{ci}) of crack growth; (2) stress associated with permanent axial deformations (σ_{cd}) or unstable crack growth and long-term strength as defined by Bieniawski (1967); and (3) the peak (σ_f) or maximum stress (see Fig. 3). For the unconfined case the peak strength is generally referred to as σ_c and has become the standard index test for establishing the short-term laboratory compressive strength. However, as noted by Hudson et al. (1972) and Martin and Chandler (1994), σ_c is not a material property but is controlled by the boundary conditions of the test.

The three stress levels referred to above represent important stages in the development of the macroscopic failure process. The early work by Brace et al. (1966) showed that the onset of

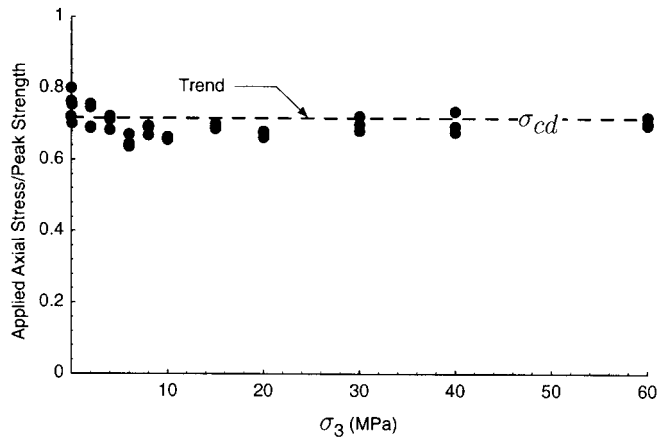
Fig. 5. The development of a failure plane in a confined sample ($\sigma_3 = 55$ MPa). Data from Lockner et al. (1992). Note that from the volumetric strain curve the initiation of the growth of failure plane starts after the characteristic reversal in slope. mstrain, microstrain.



cracking, i.e., damage, in low-porosity rocks (aplite, basalt, diabase, granite, marble, quartzite, monzonite, and soapstone) and concretes initiated at uniaxial loads between 0.3 and $0.5\sigma_c$. The microscope work by Tapponnier and Brace (1976) has shown that the length of these cracks, at this stage in the damage process, is approximately equal to the grain size of the rock. As the loads are increased beyond this crack-initiation stress level the damage to the sample accumulates and when a critical crack density is reached macroscopic failure of the sample initiates. Lockner et al. (1992) have suggested that the macroscopic failure of the sample initiates when crack interaction can occur and in confined laboratory tests they found that this occurs when the ratio of the spacing between the crack centres to the crack length is <1 . When this critical crack density is reached laboratory samples display macroscale dilation and the stress level associated with this critical crack density is easily seen in the volumetric strain curve where the curve shows its characteristic reversal in slope between 0.7 and 0.8 of the peak strength (Fig. 3).

Once failure initiates, brittle rocks, such as Lac du Bonnet granite, show significant strain softening in the postpeak region (Fig. 4). This strain-softening behaviour is characteristic over the range of confining stresses which is of interest for civil engineering and deep-mining applications. The large stress drops that are measured in the postpeak region, immediately beyond the peak, are associated with the macroscale failure of the laboratory samples. Lockner et al. (1992) used acoustic emission to track the development of a macroscale failure plane

Fig. 6. The relationship between the long-term strength (σ_{cd}) as a function of confining stress (σ_3). The long-term strength is normalized to the peak strength for the corresponding confining stress.



in a confined sample. Figure 5 shows that a narrow failure plane develops over a small axial displacement increase and the failure process initiates after the volumetric strain shows its characteristic reversal in slope at about 0.7 of the peak strength and is essentially completed by the end of the first major stress drop beyond the peak strength (stage f in Fig. 5).

More recently, Martin and Chandler (1994) argued that the stress level associated with the macroscale dilatancy, that typically occurs at stress levels above 0.7 of the peak strength, represents the initiation of failure by sliding along a macrocrack, as the axial strains become permanent at this stage of the laboratory test. And, as shown in Fig. 6, the stress level associated with the initiation of failure, when normalized to the peak strength, is independent of the confining stress.

Although the peak strength represents the ultimate capacity of the sample, the damage process, which ultimately leads to brittle failure, initiates long before the peak strength is reached. In unconfined samples, the damage initiates at about 0.4 of the uniaxial strength. Unlike the stress associated with volumetric strain reversal, the damage-initiation stress is difficult to determine from the stress-strain curves under confined conditions. Scholz (1968), Holcomb and Martin (1985), and Pestman and Van Munster (1996) studied the crack initiation of granite, sandstone, and marble using acoustic emission techniques. Their results indicate that, for confined conditions, the damage-initiation surface, in σ_1 - σ_3 space, can be approximated by

$$[1] \quad \sigma_1 = 0.4\sigma_c + 1.5 \text{ to } 2\sigma_3$$

Recent acoustic emission studies by F. Homand (personal communication) on laboratory samples under confined conditions have shown that damage initiation for Lac du Bonnet granite can be approximated by

$$[2] \quad \sigma_1 = 72 \text{ MPa} + 1.5\sigma_3$$

Regardless of the slope of the damage surface under confined conditions, the damage process in Lac du Bonnet granite involves the accumulation of cracks that extend in the direction of the maximum applied load and that for unconfined laboratory samples this process initiates between 0.3 and $0.4\sigma_c$.

To track the influence of these cracks, i.e., crack-induced

Fig. 7. Damage (ϵ_v^p) is defined as permanent volumetric strain.

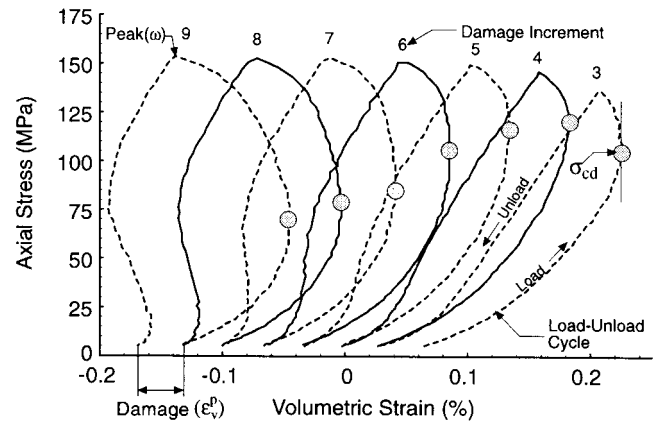
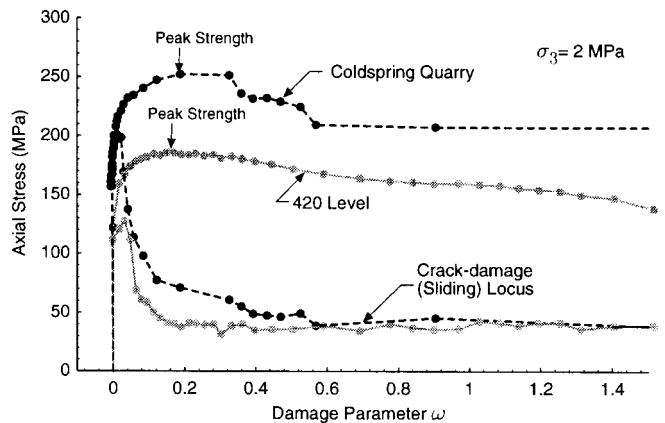


Fig. 8. Crack-damage (sliding) locus and peak strength versus the damage parameter ω . Note the major drop in the crack-damage locus before the peak strength is reached.



damage, on the failure process Martin (1993) analyzed a unique set of 37 damage-controlled laboratory tests. The samples were obtained from the 420 Level of URL. Each sample was subjected to a series of load-unload cycles and the permanent volumetric strain (ϵ_v^p) recorded. A damage parameter (ω) was defined as the cumulative permanent volumetric strain (Fig. 7):

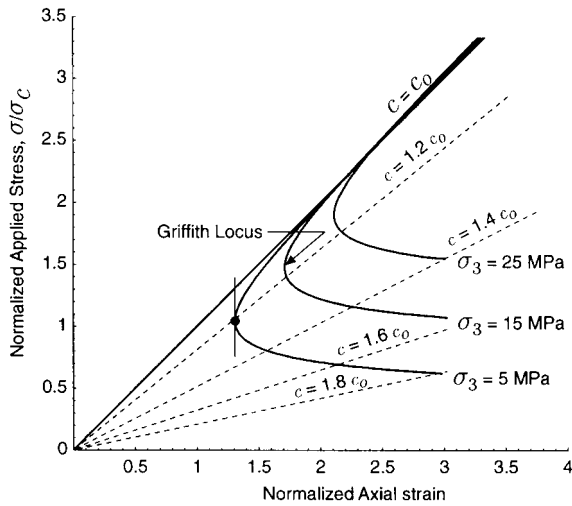
$$[3] \quad \omega = \sum_{i=1}^n (\epsilon_v^p)_i$$

Martin (1993) showed that as the crack-induced damage accumulated in the sample, the stress level associated with crack initiation remained essentially unchanged but the stress level required to initiate sliding reduced dramatically (Fig. 8). Note that in Fig. 8 the rapid decrease in the stress required to initiate sliding as damage accumulates decreases before the peak strength of the sample is reached. Martin and Chandler (1994) compared the sliding locus obtained from the damage-controlled test to the theoretical Griffith locus of sliding proposed by Cook (1965). A brief review of this work follows.

Griffith locus of sliding

Starr (1928) derived the equation for shear displacement of a zero-width crack of length $2c$ as a function of the driving shear

Fig. 9. Example of the effect of confining stress (σ_3) on the Griffith locus.



stress (S). The average relative shear displacement (U_s) of the two crack surfaces is given by

$$[4] \quad U_s = \frac{\pi}{2} (1 - \nu) S \frac{c}{G}$$

where ν is Poisson's ratio, and G is the shear modulus. Starr further demonstrated that the reduction in elastic strain energy (W_e) during crack shear displacement is given by

$$[5] \quad W_e = \frac{\pi}{2} (1 - \nu) S^2 \frac{c^2}{G}$$

and the critical condition for crack extension is

$$[6] \quad S \geq 2 \left(\frac{\alpha G}{\pi(1 - \nu)c} \right)^{1/2}$$

where α is the crack surface energy.

For the compressive loading case, Cook (1965) replaced S with $(\tau - \mu\sigma_n)$ in [5] (see definitions below) and equated the work done at the external boundaries (WD) of a material containing an inclined crack to the stored elastic strain energy in the material due to the external loads (SE), the elastic strain energy associated with shear displacement (W_e), plus the work done against friction forces (W_f):

$$[7] \quad WD = SE + W_e + W_f$$

Martin and Chandler (1994), using the approach of Cook, showed that for the confined case the axial strain ϵ for the sliding-crack model is given by

$$[8] \quad \epsilon = \frac{\sigma_1 - 2\nu\sigma_3}{2G(1 + \nu)} + \frac{2}{(\sigma_1 - \sigma_3)} \left(W_s + \frac{W_f}{2} \right) n$$

where

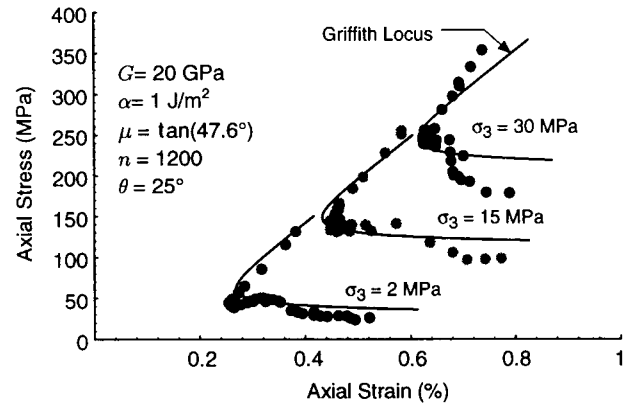
$$W_s = \frac{\pi}{4} (1 - \nu) \frac{S^2}{G} c^2$$

$$W_f = \frac{\pi}{2} (1 - \nu) \mu \sigma_n \frac{S}{G} C^2$$

$$S = \tau - \mu\sigma_n$$

n is the crack density, and τ and $\mu\sigma_n$ are defined by equations

Fig. 10. Comparison of the calculated theoretical Griffith locus (solid line) and the measured Griffith locus at confining stresses of 2, 15, and 30 MPa.



9 and 10. Note that the axial strain is a function of both the crack length and the crack density. If either the crack density or the crack length goes to zero, [8] recovers the elastic modulus of the undamaged material. Hence, [8] tracks the effect of cracks on the modulus of the rock (Fig. 9). The condition for sliding occurs when [6] is satisfied and the critical axial strain (Griffith locus) is obtained by substituting the value of c in [6] into [8]. As a rock containing a crack density is loaded, it will follow a stress-strain path dictated by its effective modulus, for that crack density. When the stress-strain path intersects the Griffith locus, crack extension will occur. It is important to note that, for a given crack length, the crack can respond in a stable or unstable manner. For example, if the stress-strain path intersects the Griffith locus to the left of the vertical tangent to the locus, unstable fracture propagation will occur, whereas a stress-strain path intersection to the right of the vertical tangent results in stable fracture propagation (Fig. 9). Thus an unstable crack can extend and become stable under some loading paths.

The Griffith locus of sliding given by [8] was compared with results from the damage-controlled tests at confining stresses of 2, 15, and 30 MPa. The model was first calibrated to an unconfined test to determine the crack density n and then the confining stress was increased (Fig. 10). It should be noted that, for the comparison in Fig. 10, the value of α was assumed and the crack density back-calculated. Thus, the crack density can vary significantly depending on the value of α . Despite the uncertainty in the value of α , the agreement between the measured and the predicted loci is quite good at all confining stresses.

For the conditions of triaxial compression and assuming that the crack plane is parallel to the direction of the intermediate compressive stress, the value of σ_1 corresponding to the critical condition for sliding can be derived by replacing S with $(\tau - \mu\sigma_n)$ in [6] and substituting:

$$[9] \quad \sigma_n = \frac{\sigma_1 + \sigma_3}{2} - \frac{\sigma_1 - \sigma_3}{2} \cos 2\theta$$

$$[10] \quad \tau = \frac{\sigma_1 - \sigma_3}{2} \sin 2\theta$$

where θ is the angle between the critical crack surface and

Fig. 11. Effect of increasing crack length on cohesion given by [11].

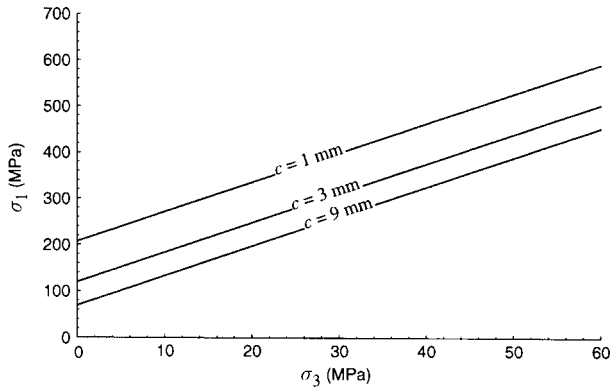
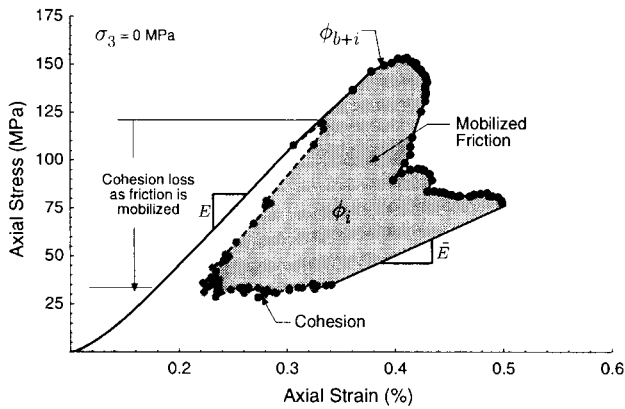


Fig. 12. Mobilization of friction and cohesion as a function of axial strain.



the direction of the maximum applied stress (σ_1), and μ is the coefficient of friction. Failure (σ_1) can then be expressed in σ_1 - σ_3 space as

$$[11] \quad \sigma_1 \geq 2 \left(\frac{\alpha G}{\pi(1-\nu)c} \right)^{1/2} \tan \left(45 + \frac{\phi}{2} \right) + \sigma_3 \tan^2 \left(45 + \frac{\phi}{2} \right)$$

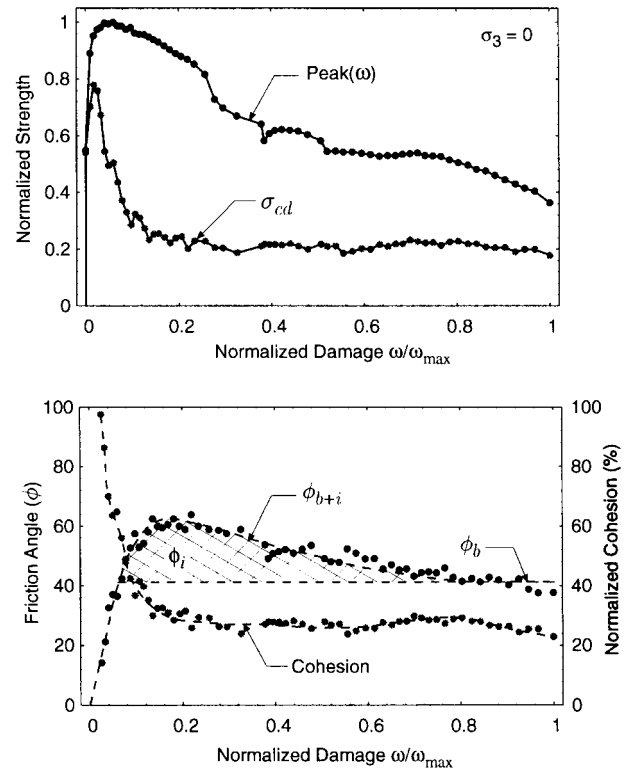
Equation [11] is identical to the classical Rankine equation for shear failure based on the Mohr-Coulomb failure criterion given by

$$[12] \quad \sigma_1 = 2S_0 \tan \theta_c + \sigma_3 \tan^2 \theta_c$$

where θ_c is the critical angle for shear, and S_0 is the rock mass cohesion. An examination of [11] reveals that the fracture surface energy and crack length only apply to the cohesive component of the material and that the frictional strength is not dependent on these parameters. Thus small extensions of the crack can dramatically decrease the cohesion of a brittle rock (Fig. 11).

The Griffith locus of sliding was used by Martin and Chandler (1994) to track the mobilization of friction and the progressive loss of cohesion as a sample fails (Fig. 12). The concept of cohesion loss can only be explained in this manner if nonelastic deformations are required to mobilize friction and if the friction component is made up of a residual component (ϕ_b) and an interlocking or dilation component (ϕ_i), such that the total frictional resistance can be expressed as ϕ_{b+i} . Figure 13

Fig. 13. Mobilization of friction and cohesion as a function of normalized damage.



shows the mobilization of friction and resulting cohesion loss as a function of damage. Note that, in Fig. 13, the damage has been normalized to the maximum damage recorded at the end of the test and the strength has been normalized to the peak strength.

Cracks and laboratory properties

In the preceding section it was shown that the cohesive strength component is a function of damage and that this damage can be approximated by the stress-strain response of a cracked elastic material. The fundamental assumption in the development of the Griffith locus concepts is the sliding-crack model. For these analyses it is assumed that the cracks are self-consistent and that the elastic properties are the average properties of the cracked material. To account for the combined effect of crack length (c) and crack density (n), a crack-density parameter $\lambda = Nc^2/V$ will be used, where N/V is the number of cracks in the total volume (Kemeny and Cook 1986). The effective modulus (\bar{E}) is given by

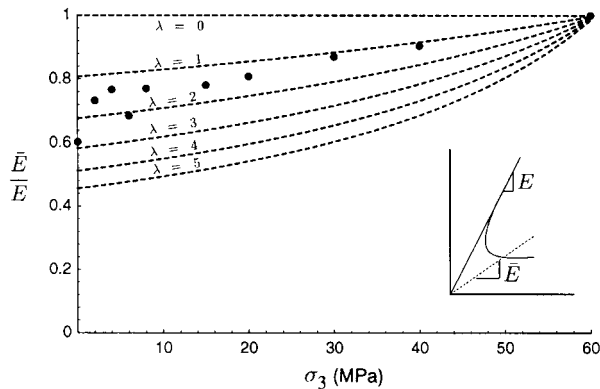
$$[13] \quad \bar{E} = \frac{\sigma_1 - \sigma_3}{\epsilon}$$

where

$$\begin{aligned} \bar{\epsilon} &= \frac{\sigma_1 - \sigma_3}{E} + \frac{2}{\sigma_1 - \sigma_3} \left(W_s + \frac{W_f}{2} \right) \lambda \\ W_s &= \frac{\pi}{2} (1 - \nu^2) \frac{(\tau - \mu\sigma_n)^2}{E} \\ W_f &= \pi(1 - \nu^2) \mu\sigma_n \frac{(\tau - \mu\sigma_n)}{E} \end{aligned}$$

Figure 14 shows the effective Young's modulus normalized

Fig. 14. The effect of the confining stress (σ_3) on the effective Young's modulus (\bar{E}) normalized to the initial Young's modulus (E) for crack-density parameters (λ).



to the initial modulus without any cracks as a function of confining stress for various values of λ . Also shown in Fig. 14 is the measured effective modulus as the Griffith locus reaches its plateau value in Fig. 10. Again the agreement between the predicted and measured values is good, suggesting that the sliding-crack model has merit for analyzing the failure process in laboratory compression tests. However, microcracking starts in laboratory compression tests at stress values of about 0.3–0.5 of the peak strength which is considerably lower than when the initiation of sliding occurs. The effect of these cracks on laboratory properties was investigated by Martin and Stimpson (1994).

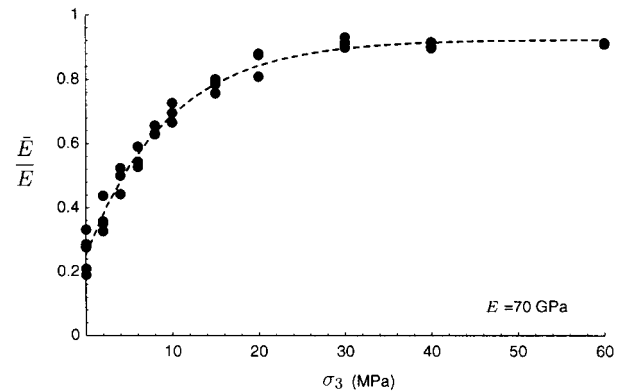
Martin and Stimpson (1994) showed that samples of Lac du Bonnet granite were subject to sample disturbance. This sample disturbance results from microcracks that develop during the sampling (unloading) process. They showed that the effect of these microcracks is to reduce the cohesive strength of the material, both in tension and compression, and to reduce the Young's modulus. They also showed that reduction in these properties was related to the ratio of the maximum far-field in situ stress magnitude (σ_1) to the undamaged unconfined compressive strength, σ_c (i.e., the larger the ratio σ_1/σ_c , the greater the damage). For Example, Fig. 8 shows the difference in the peak strength for a sample obtained from the 420 Level of URL where the ratio σ_1/σ_c is approximately 0.3 compared with <0.1 for a sample taken from Coldspring Quarry.

The effect of unloading damage on prepeak properties is also illustrated in Fig. 15, which shows the secant Young's modulus taken at 50% of the peak load for various confining stresses for samples also taken from the 420 Level of URL. Unlike Fig. 14, Fig. 15 shows a very strong dependence on confining stress. It is obvious that the sliding-crack model (post-peak) used in the development of Fig. 14 does not describe the prepeak damage process that occurs by taking a sample from the stressed rock mass. One of the reasons for this discrepancy is the different loading paths experienced by the samples. This difference will be explored in the sections which follow.

Summary

In compression tests, the start of failure coincides with the initiation of damage caused by small cracks growing in the direction of the maximum applied load. For unconfined Lac du Bonnet granite, this occurs when the stress magnitudes reach about 0.3 to 0.4 σ_c . The rock can carry additional load, as this

Fig. 15. The effect of confining stress on the secant Young's modulus normalized to the undamaged Young's modulus.



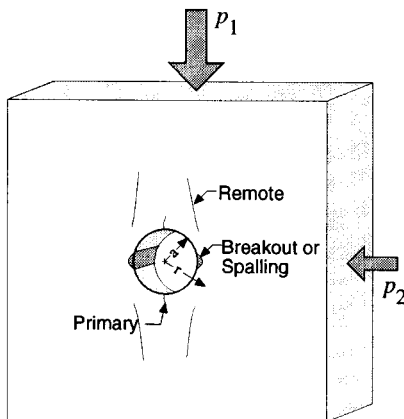
damage process is stable. Eventually, when the rock sample contains a sufficient density of these stable cracks, they start to interact and a transition from a stable to an unstable cracking (sliding) process occurs. For Lac du Bonnet granite, this transition occurs when the deviatoric compressive stress reaches about 0.7 σ_c . Constant loads above this stress level cannot be sustained and failure eventually occurs (Martin and Chandler 1994; Schmidtke and Lajtai 1985). For the unconfined case this level, called the long-term strength of the rock, for undisturbed samples of Lac du Bonnet granite is about 160 MPa. Thus if a sample is subjected to a loading process which causes damage, the strength of that sample, particularly the unconfined strength, is significantly reduced. For small amounts of damage, this cohesion loss can amount to 50% or more of the initial cohesion of the sample. Similar findings for soils have been reported by Schmertmann and Osterberg (1960).

The damage process can occur when a sample is monotonically loaded beyond crack initiation or when a sample is taken (unloaded) from the stressed rock mass. The unloading damage process is more effective at low confining stresses in reducing the cohesion-related properties, i.e., Young's modulus, of the rock and this reduction occurs before the laboratory peak strength is reached. This difference between loading and unloading will be explored in the following sections. In the next section the strength around circular openings in physical models is investigated.

Rock strength around circular openings in physical models

The most prominent failure zone observed around circular openings in brittle rocks is the region of breakout or spalling. This zone forms as a V-shaped notch on opposite sides of opening. Researchers, e.g., see Lajtai et al. (1991) and Hoek (1965), using physical model studies have identified two other types of fractures around circular openings, namely tensile or primary fractures, and secondary or remote fractures (Fig. 16). Hoek (1965) carried out biaxial compression tests on chert and noted all three types of fractures around a 19 mm diameter circular opening. Martin (1993) carried out a similar test in Lac du Bonnet granite and also found all three types of fractures around a 60 mm diameter circular opening. The breakouts occur in the region of maximum tangential stress (σ_θ) around the boundary of the circular opening, which for plane-strain conditions is given by (Jaeger and Cook 1979)

Fig. 16. Types of fractures found around circular openings in laboratory model tests.



$$[14] \quad \sigma_{\theta} = \frac{p_1 + p_2}{2} \left(1 + \frac{a^2}{r^2} \right) + \frac{p_1 - p_2}{2} \left(1 + \frac{3a^4}{r^4} \right)$$

where p_1 and p_2 are the applied loads (Fig. 16), a is the radius of the opening, and r is the radial distance to the point of interest. At the boundary of the opening $a = r$ and $\sigma_{\theta} = 3p_1 - p_2$, where $p_1 > p_2$. For the unconfined case, $p_2 = 0$ and the maximum tangential stress at the breakout is $3p_1$.

The effect of size and stress gradients on the breakout strength around boreholes has been examined by many researchers using various physical models, e.g., Carter (1992), Ewy and Cook (1990), Haimson and Herrick (1989), Mastin (1984), and Hoek (1965). One of the commonly reported outcomes of such tests is that the tangential stress at the boundary of the borehole required to cause breakouts is at least twice the unconfined compressive strength of the material. Carter (1992) and Haimson and Herrick (1989) conducted an extensive series of tests on limestone using circular openings which ranged in diameter from 6.4 to 110 mm. The tests consisted of loading in uniaxial compression and monitoring, using strain gauges, when breakouts occurred. Figure 17 is a summary of the results from Haimson and Herrick (1989) and Carter (1992) and the results from Mastin (1984) for Berea Sandstone. Their results show that as the borehole size increases the tangential stress at failure approaches the unconfined compressive strength of the material but that a significant strength-scale effect is observed for boreholes less than 75 mm in diameter. For borehole diameters of less than 20 mm, the tangential stress required to initiate breakouts is greater than $2\sigma_c$.

A set of tests similar to those reported above was carried out to investigate the effect of borehole diameter on the side-wall stress required to initiate breakouts in samples of Lac du Bonnet granite. Thirteen unconfined samples were tested with circular openings ranging in diameter from 5 to 103 mm. Strain gauges were used to monitor the deformations and to determine the onset of breakouts (Martin 1993). The placement of strain gauges on each sample was modified depending on sample size. The results from the 13 tests are also plotted in Fig. 17. These results generally agree with those of Carter (1992) and Haimson and Herrick (1989).

Lajtai (1972) and Carter (1992) proposed that the strength-scale effect observed in Fig. 17 was related to the microcracking

Fig. 17. Summary of uniaxial testing of blocks containing a circular borehole.

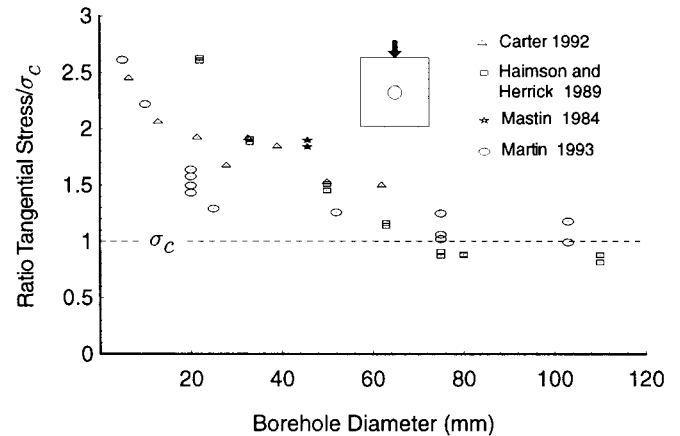
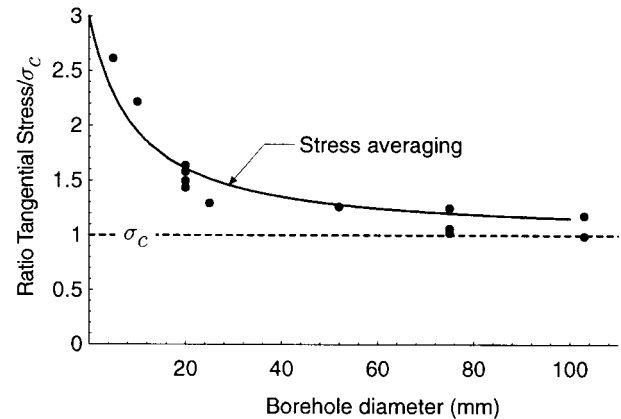


Fig. 18. Tangential stress required to cause borehole breakouts in Lac du Bonnet granite compared with the strength predicted by [15].



occurring in the region of high stress gradients and could be approximated by a stress averaging technique given by

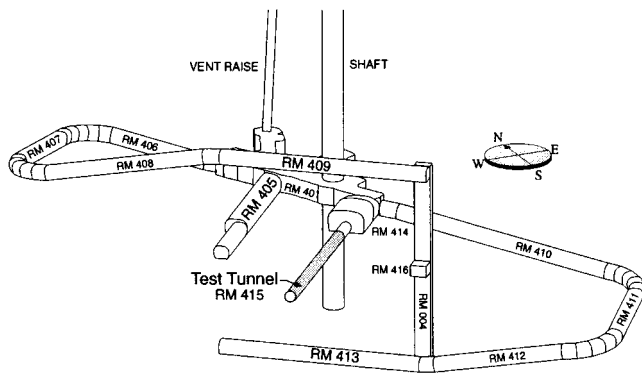
$$[15] \quad \bar{\sigma}_{\theta} = \frac{p(a+t)}{t} \left\{ 1 - \frac{a^2}{2(a+t)^2} - \frac{a^4}{2(a+t)^4} \right\}$$

where $\bar{\sigma}_{\theta}$ is the average maximum tangential stress for a borehole subjected to a uniaxial load p , a is the borehole diameter, and t is the distance over which the tangential stress is averaged. Equation [15] was fitted to the Lac du Bonnet granite data and the results are shown in Fig. 18 where $t = 14$ mm.

What is most obvious in Figs. 17 and 18 is the significant increase in the tangential stress required to cause breakouts for boreholes less than about 75 mm in diameter. Because most laboratory studies are carried out with borehole diameters of 25 mm or less, a scale effect of at least 2 should be anticipated when comparing the ratio of tangential stress required to cause breakouts to the unconfined compressive strength (Fig. 17). However, it would appear that when the borehole is at least 75 mm in diameter, the strength is close to the unconfined compressive strength and the apparent scale effect is either absent or significantly reduced.

The phenomenon of increased strength around small-diameter boreholes has also been reported for samples tested in biaxial

Fig. 19. General layout of the excavations on the 420 Level and the Mine-by test tunnel. The test tunnel has an azimuth of 225°.



and polyaxial loading. Lee and Hamimson (1993) carried out polyaxial testing of forty 100 mm cubes of Lac du Bonnet granite containing a 21 mm diameter borehole. They also found that the tangential stress required to initiate breakouts varied from 1.5 to $2\sigma_c$. Martin (1993) tested one block of Lac du Bonnet granite containing a 60 mm diameter borehole using a biaxial loading system and found that the tangential stress required to initiate breakouts occurred at $1.6\sigma_c$. The results of Lee and Hamimson (1993) and Martin (1993) are in keeping with the scale effect shown in Fig. 17. It appears that the strength-scale effect is not related to the type of loading conditions, i.e., one-, two-, or three-dimensional. In the next section, the in situ failure process around circular openings is examined.

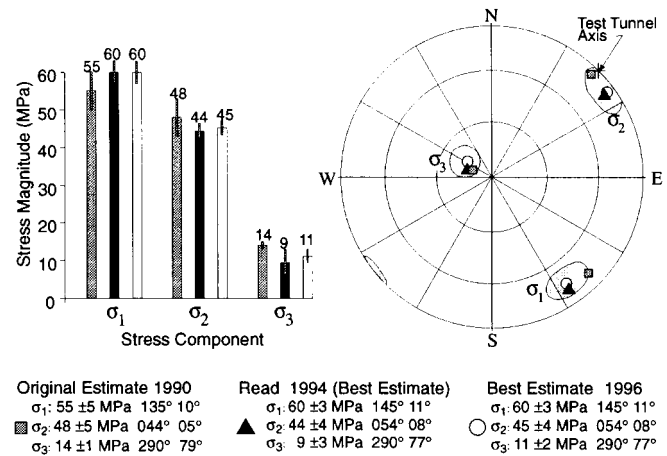
Rock strength around circular openings in situ

As stated in the introduction, the in situ study was carried out at the 420 Level of URL in massive granite. To carry out the Mine-by Experiment, approximately 500 m of access tunnel was required (Fig. 19). These tunnels were typically horse-shoe-shaped and excavated using drill-and-blast techniques. These tunnels provided excellent visual observations of the rock mass response, as the tunnels were excavated in different directions relative to the in situ stress tensor.

Far-field stress state

The in situ stresses at the URL have been investigated extensively (Martin 1990) and three distinct stress domains have been defined (Martin and Chandler 1993). At the 420 Level (domain III), the in situ stress magnitudes are $\sigma_1 = 60 \pm 3$, $\sigma_2 = 45 \pm 4$, and $\sigma_3 = 11 \pm 2$ MPa, and σ_1 trends about 145° and plunges 11–14°. Figure 20 compares the in situ stresses estimated at the beginning of the experiment and those determined at the end of the experiment by back-analyses. The Mine-by test tunnel was originally intended to be oriented parallel to the trend of σ_2 to maximize the stress concentrations around the tunnel. Figure 20 shows that the trend of the tunnel is off the trend of σ_2 by about 10°, and deviates about 8° in plunge. Although for most practical purposes this difference in orientation would not be considered important, it does impact on the interpretation of results, as will be shown in the section Initiation of the cohesion-loss process.

Fig. 20. Summary of the estimated in situ stresses for the 420 Level. The grey circular areas in the stereonet and the small bars in the histogram are the 90% confidence interval for the orientation and magnitude, respectively. The estimates are given as magnitude, trend, and plunge.



In situ strength

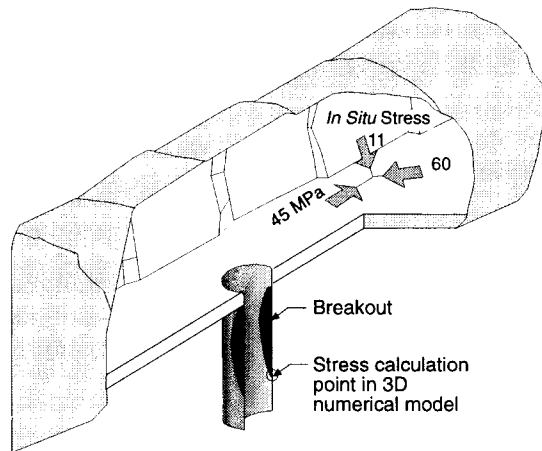
To determine if the strength-scale effects observed in the laboratory were present in situ, a series of vertical boreholes with diameters of 75, 150, 300, 600, and 1250 mm were diamond drilled to a nominal depth of 5 m from the floor of Room 405 at URL (Figs. 19 and 21). In addition, a 46 m long, 3.5 m diameter tunnel was excavated, without the aid of explosives, as part of the Mine-by Experiment (Read and Martin 1992) and is shown as the test tunnel in Fig. 19.

Borehole breakouts, if present, formed immediately during the drilling of the boreholes and excavation of the test tunnel. The breakouts in the boreholes extended from the floor of Room 405 to various lengths depending on the diameter of the borehole, i.e., the larger the borehole diameter, the longer the breakout, suggesting a scale effect (Martin et al. 1994). The lengths of the breakouts were recorded immediately after drilling and are still being monitored. Only minor changes in the length of the breakouts have been observed after nearly 2 years of monitoring.

The stress concentrations below the floor of Room 405 decrease with the depth along each borehole. Thus the tangential stress at the end of each breakout will also vary. An elastic three-dimensional stress analysis of Room 405 and each borehole in the floor was carried out using Examine^{3D} (Curran and Corkum 1995b) to determine the maximum tangential stress at which the borehole breakout stopped (Fig. 21). This stress value was considered equivalent to the tangential stress at the initiation of borehole breakout in the laboratory studies. A comparative analysis was carried out on the test tunnel to determine the effect of including the breakout geometry on the calculated stress. This analysis showed that the change in the tangential stress, caused by the breakout geometry, was less than 10% at the point of interest. In all the analysis reported here, the geometry of the breakout was not included. Also, all the boreholes were drilled close to the centre of the 5 m wide excavation to minimize any stress concentration occurring near the edges of the excavation.

Figure 22 shows the calculated maximum tangential stress required to initiate breakouts normalized to σ_c for the

Fig. 21. Illustration of the three-dimensional geometry used to calculate the stress at the borehole breakout.



borehole diameters investigated. Also shown, for comparative purposes, are the laboratory data from Fig. 18. Figure 22 shows a modest effect of scale for the in situ data and a noticeable change in the effect of scale between the laboratory and in situ results. This is also supported by the observation that a 75 mm diameter borehole drilled near the centre and in the same direction as the test tunnel also showed breakouts similar to those observed in the test tunnel (horizontal holes in Fig. 22). The in situ results also suggest that the in situ strength may be related to the direction of the holes relative to the stress state. Nonetheless, all the in situ results suggest a modest strength-scale effect.

The boreholes were drilled about 11° from the direction of σ_3 and were subjected to the stress concentrations resulting mainly from σ_1 and σ_2 . The test tunnel, however, was excavated essentially parallel to σ_2 and was subjected to the stress concentrations caused by mainly σ_1 and σ_3 . The ratio σ_1/σ_3 at the location of the test tunnel is greater than 3, which should result, according to elastic theory, in the formation of tensile cracks in the walls of the tunnel. Inspection of the tunnel walls did not find any tensile cracks at a scale visible to the naked eye. In fact, inspection of all excavations and boreholes on the 420 Level excavated without the aid of blasting did not locate any continuous tensile cracks.

An observation trench was excavated in the floor of the test tunnel several months after the test tunnel was completed. The trench was excavated to a depth of about 2 m for the full width of the tunnel. Careful inspection of the breakout exposed by the trench did not find any trace of a remote fracture as observed in the laboratory physical models. Thus the primary (tensile) and remote fracture patterns observed in the laboratory are not noticeable in situ at the stress levels found at the 420 Level.

Failure process around the Mine-by test tunnel

The 46 m long, 3.5 m diameter Mine-by test tunnel was excavated between January and July 1992. The test tunnel had a circular profile and was excavated in the azimuth direction of 225°, approximately parallel to σ_2 (Fig. 19). This configuration provided the maximum stress concentration in the roof

Fig. 22. Ratio of the calculated tangential stress to σ_c at which breakouts initiate for various borehole diameters.

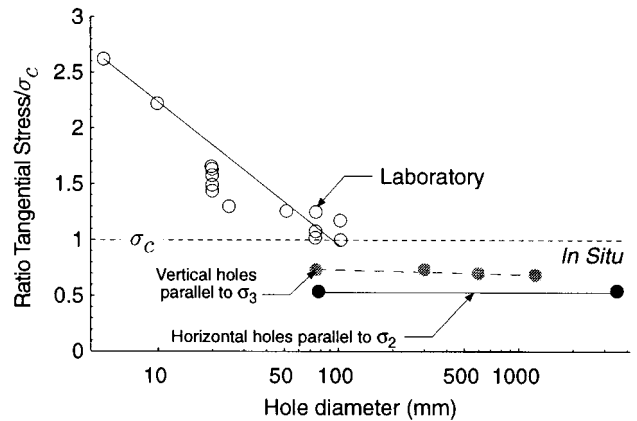
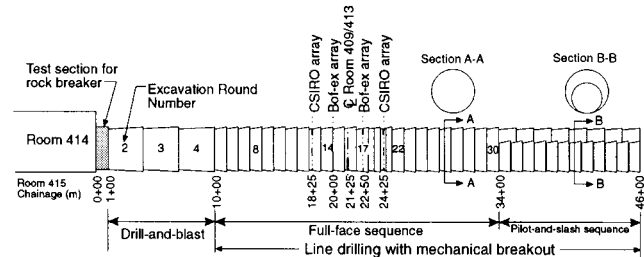


Fig. 23. Section through the Mine-by test tunnel (Room 415) showing the excavation methods and sequence used for the Mine-by Experiment.

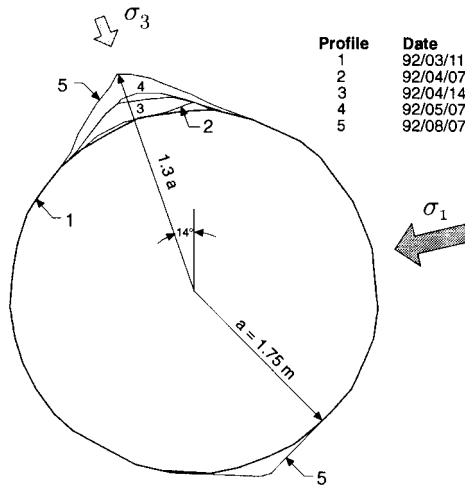


and floor of the tunnel. The tunnel was excavated in 1 and 0.5 m increments (Fig. 23) using perimeter line drilling and mechanical breaking of the central rock stub (Onagi et al. 1992). Excavation was carried out daily in two 8 h shifts, but experimental activities constrained progress to one round about every 3 days. The temperature of the test tunnel was maintained within 1.5° of the ambient rock temperature of 10.5°C and >90% relative humidity by an air conditioning unit. Extensive state-of-the-art geomechanical instrumentation, installed prior to the start of the excavation, was used to monitor the complete mechanical response of the rock mass around the tunnel (Read and Martin 1992). The excavation method also provided an ideal environment in which to observe and record the brittle-failure process.

Shape of failure zone

Spalling, i.e., failure, in the roof and floor of the test tunnel was observed immediately as each excavation round was taken, and failure progressed radially as the test tunnel face was advanced. The spalling process occurred within about two diameters of the advancing tunnel face and resulted in the formation of a V-shaped notch in the regions of maximum tangential stress. Figure 24 illustrates the development of the notch in the roof over about a 5 month period at a monitoring station referred to as round 17 (see Fig. 23 for location). The progressive development of the notch in the floor could not be observed because the floor always contained “tunnel muck” until the tunnel advance was completed. The size and development of the notch were monitored at six stations. In all cases the shape

Fig. 24. Progressive development of the notch geometry in the roof and floor of the Mine-by test tunnel at Round 17 over a 5 month period.



of the notch was nearly identical and the radial depth of the notch in the roof, measured from the centre of the tunnel, varied from 1.3 to 1.5a, where a is the tunnel radius.

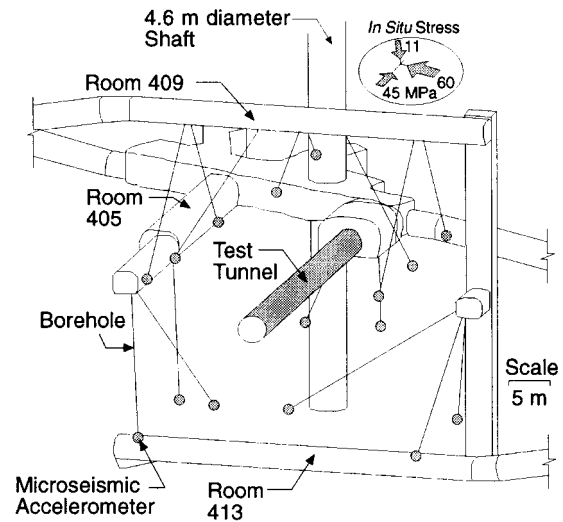
Spatial location of microseismic events

It is well known that cracking occurs around an opening excavated in a highly stressed brittle rock. Earlier work at URL had established that considerable microseismic activity was associated with the excavation, by drill-and-blast techniques, of a circular shaft from the 240 Level to the 420 Level (Talebi and Young 1992). The test tunnel for the Mine-by Experiment was excavated without the use of blasting and this provided a means to determine if the microseismic activity was associated with blasting or simply related to stress redistribution.

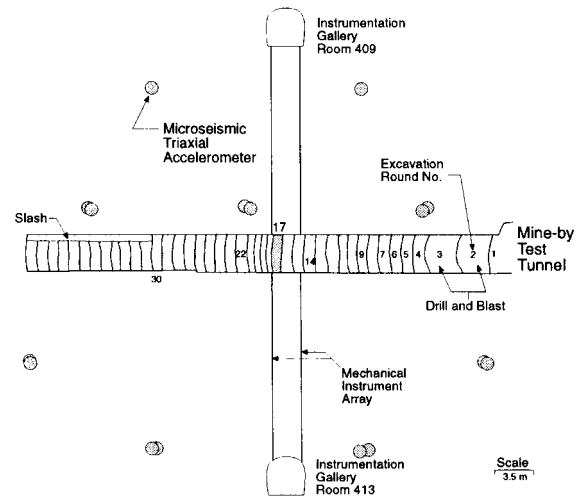
An array of 16 triaxial accelerometers was installed to monitor the microseismicity associated with the excavation of the test tunnel (see Fig. 25). The accelerometers were grouted in place at the end of diamond-drilled boreholes (Fig. 25a). The accelerometer array was designed for focal sphere coverage and a source location accuracy of about ±0.25 m near the centre of the tunnel. The sampling rate was set to 50 kHz and the overall system frequency response was 50 Hz to 10 kHz (±3 dB). The dynamic range of the system allowed the study of seismic events with moment magnitudes as small as -6. The sequencing of the construction schedule for the test tunnel provided about 12 h of quiet time for microseismic monitoring after the initial perimeter drilling and about 12 h of quiet time for microseismic monitoring after mechanical breaking of the rock stub. This provided a total of about 24 h of monitoring per round of tunnel advance.

Preliminary processing of the microseismic data was carried out in the field using automated source location computer software developed at Queen’s University (Collins and Young 1992). Over 25 000 events were detected and some 3500 events were source located using the Queen’s University computer software (Fig. 26). Note that the clustering of events in the roof and floor in Fig. 26 indicates that the maximum stress is as measured, i.e. inclined relative to the horizontal. Figure 26 is a compilation of the information obtained from each round

Fig. 25. Location of the microseismic biaxial accelerometers distributed around the 3.5 m diameter test tunnel. (a) Layout at 420 Level. (b) Vertical section.



(a) 420 Level Layout



(b) Vertical Section

advance, and Fig. 27 shows the typical detailed source locations obtained for each round. Only the microseismic events between tunnel chainage 10.51–34.28 m are discussed here (rounds 6–30, see Figs. 25a and 26), as the stress conditions, geology, and excavation sequence are more complex near the ends of the test tunnel.

Each excavation round between chainage 10.51 m and 34.28 m was processed individually, and the location of each microseismic event relative to the tunnel face position (X) is normalized with respect to the tunnel diameter (2a). Only those microseismic events recorded in the roof of the test tunnel are summarized here, as the formation of the roof notch was not constrained by construction activities. However, analyses of the complete data set show similar trends for the roof and floor notches (Collins et al. 1994). Figure 28 shows the distribution

Fig. 26. Location of the computer-picked microseismic events for the test tunnel plotted on an unrolled perimeter map and the location of the sample volume chosen for a detailed analysis. Also shown is the extent of the notch plotted on an unrolled perimeter map.

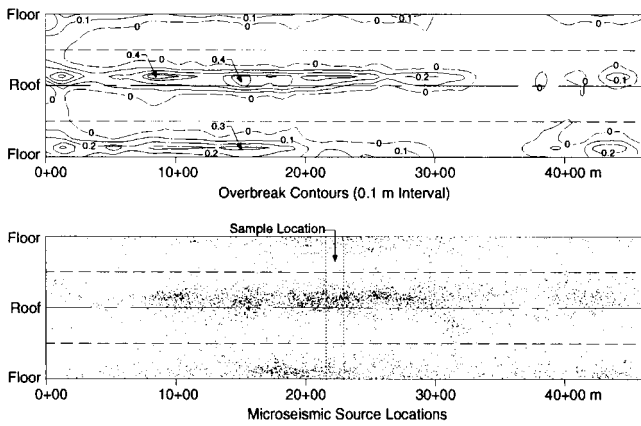
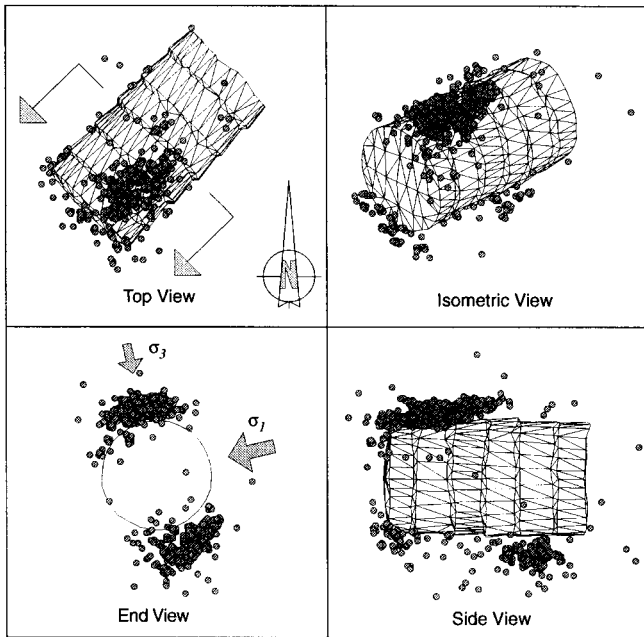


Fig. 27. Location of microseismic events for Round 17, located near the centre of the test tunnel and monitored for 19 days. Note the concentration of the microseismic events near the face of the test tunnel in the region where the V-shaped notch will eventually form.



of microseismic events for rounds 6–30 relative to the tunnel face. Note the rapid decrease in microseismic activity between $-2X/2a$ and the tunnel face and that considerable microseismic activity occurs within about 0.4 diameters ahead of the tunnel face.

Source parameters relating to source strength, dimension, and stress release were calculated from the spectral parameters knowing the density of the rock mass (ρ) and the P - and S -wave velocities at the source. The seismic moment (M_0) is a measure of the strength of the seismic event and is defined as $M_0 = GAu$, where G is the modulus of rigidity at the source, A is the fault

Fig. 28. Histogram of the microseismic events recorded for rounds 6–30. The location of each event relative to the tunnel face position (X) is normalized with respect to the tunnel diameter ($2a$).

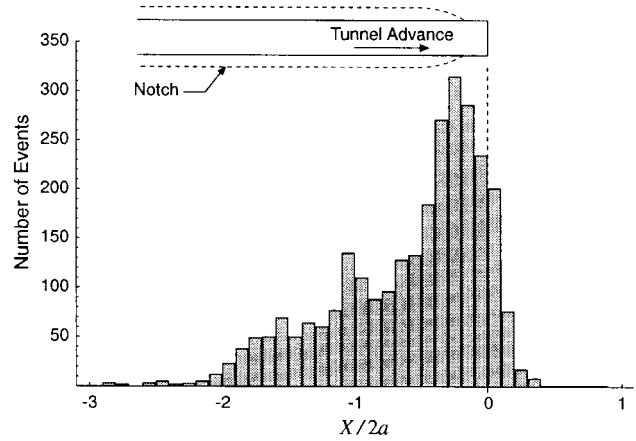
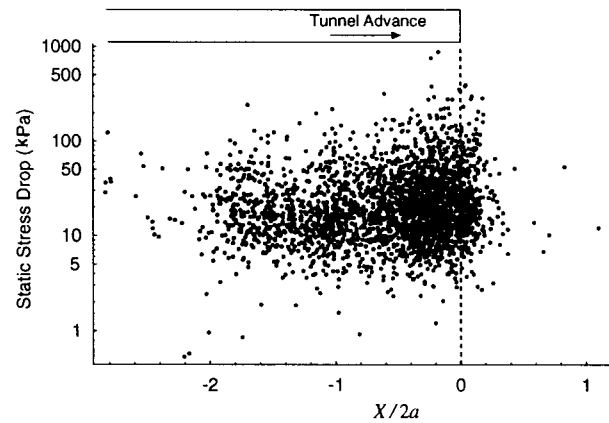
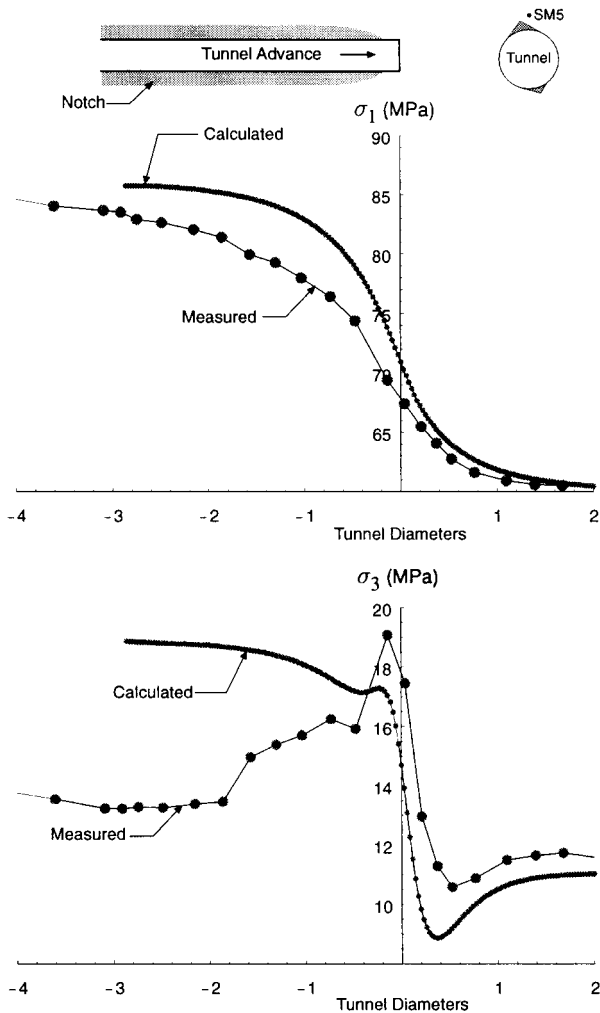


Fig. 29. Static stress drop for rounds 6–30. The location of each event relative to the tunnel face position (X) is normalized with respect to the tunnel diameter ($2a$).



area, and u is the average displacement on the fault surface (Aki and Richards 1980). In mining-induced seismicity studies, the seismic event is usually modelled as a simple circular fault, and the shear stress release at the source of the event can be estimated by the static stress drop ($\Delta\tau$), which is equal to the difference between the initial shear stress acting on the fault and the final shear stress after slip has occurred. The static stress drop can be calculated from the seismic moment and the source radius and it represents the uniform reduction in shear stress acting to produce seismic slip over a circular fault. For most mining-induced tremors the static stress drop ranges from 0.01 to 10 MPa (McGarr 1994). Figure 29 shows the static stress drop for the events recorded near the test tunnel. For the microseismic events recorded, nearly all the events fall between a constant stress drop of 200 Pa and 200 kPa, which is somewhat lower than the values given by McGarr (1994). Interestingly, most of these events are also smaller than microseismic events measured in laboratory compression tests during the development of the macroscale failure plane (McGarr 1994), suggesting that the fractures associated with

Fig. 30. Comparison of measured and calculated stress magnitudes for biaxial strain cell SM5. Note the change in the σ_3 trend at about -0.2 tunnel diameters.



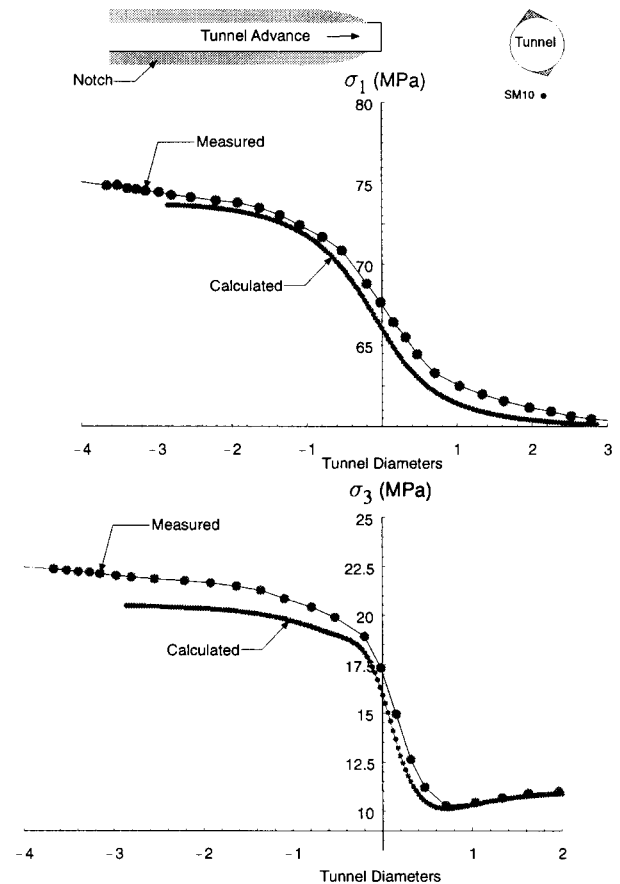
the microseismic events are probably only a few centimetres in diameter.

Initiation of the cohesion-loss process

The microseismic accelerometer array was designed for maximum source location accuracy near the centre of the tunnel (± 0.2 m). Figure 27 shows the location of the microseismic events captured when the tunnel face was advanced 1 m and monitoring continued for 19 days. There was no construction activity during this monitoring period and the temperature of the test tunnel was maintained as close to the rock temperature as possible. The laboratory compression tests showed that initiation of the cohesion-loss process occurred at about one-third to one-fifth of the unconfined rock strength. These microseismic events provided an opportunity to determine the stress level required to initiate this process in situ.

The microseismic events are an expression of the nonelastic response of the rock mass. Therefore to quantify the stress at which the in situ damage initiates, the boundary of the nonelastic region must first be defined. To determine the location of this boundary the results from three-dimensional elastic analyses

Fig. 31. Comparison of measured and calculated stress magnitudes for biaxial strain cell SM10.

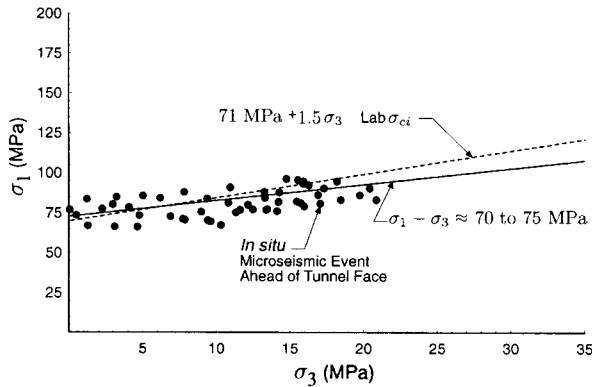


are compared with those obtained from two triaxial strain cells installed prior to the excavation of the tunnel. These cells were installed in the roof and floor and used to monitor the changes in stress magnitude and direction which occurred in the rock mass as the tunnel was excavated. A complete description of the triaxial strain equipment is given in Read and Martin (1996).

The triaxial strain cell SM5 is located in the roof of the test tunnel at a radial distance of 2.663 m (approximately 1.5 tunnel radii) from the tunnel axis. Figure 30 shows the results from the measured stress magnitudes and the stress magnitudes given by the elastic model. Ahead of the tunnel face the measured and calculated results are in good agreement, suggesting that the rock mass behaviour, ahead of the tunnel, is essentially elastic. However, inside the tunnel at about -0.2 tunnel diameters or 0.6 m from the tunnel face, the rock mass behaviour starts to deviate from the elastic response, particularly σ_3 . This finding is also supported by the observation described in the next section that the notch initiated at about 0.5–1 m from the tunnel face, also indicating the beginning of macroscale nonelastic behaviour.

The triaxial strain cell SM10 is located in the floor of the test tunnel at a radial distance of 3.394 m (approximately 1.9 tunnel radii) from the tunnel axis. Figure 31 shows the results from the measured stress magnitudes and the stress magnitudes given by the elastic model. As with SM5, ahead of the tunnel face the measured and calculated results for SM10 are in good agreement, suggesting that the rock mass behaviour, ahead of

Fig. 32. Stress associated with the microseismic events recorded ahead of the tunnel face where the rock mass response is essentially elastic. Lab σ_{ci} , laboratory in situ crack-initiation stress.



the tunnel, is also essentially elastic. However, unlike SM5 the results from SM10 also indicate that inside the tunnel the rock mass response is also essentially elastic. Thus it would appear that, once inside the tunnel, the boundary between the elastic and nonelastic responses falls between 1.5 and 1.9 tunnel radii. This value seems reasonable considering that the measured depth of the notch ranged from 1.3 to 1.5 tunnel radii.

Figure 27 shows that microseismic events, i.e., cracking, occur ahead of the tunnel face, and the results from SM5 and SM10 indicate that three-dimensional linear elastic stress analyses can be used to quantify the stress magnitudes ahead of the tunnel face. Hence, these elastic stress analyses can be used to approximate the stress magnitudes required to initiate the microseismic events (damage) ahead of the tunnel face (Fig. 32). A least squares fit to the data in Fig. 32 indicates that the in situ damage-initiation stress can be approximated by a constant-deviatoric stress given by

$$[16] \quad \sigma_1 - \sigma_3 \approx 70 \text{ to } 75 \text{ MPa}$$

The damage-initiation stress given by [16] implies that the in situ cracking starts when the maximum deviatoric stress exceeds approximately one-third the unconfined compressive strength. This is very similar to the stress magnitude associated with crack initiation in the laboratory study. There, the crack-initiation stress ranged from one-third to one-half the unconfined compressive strength. Equation [16] is also very similar to [2], which described crack initiation for laboratory-confined samples. Figure 33 shows the computed damage-initiation stress for microseismic events ahead of the tunnel face from several excavation rounds. These results also show strong clustering about the line given by [16]. Also shown in Fig. 33 is the laboratory peak strength and the laboratory long-term strength. Figure 33 shows that the cohesion-loss process initiates at stress levels well below the laboratory peak and long-term strength for undamaged samples.

Additional three-dimensional elastic stress analyses were used to compare the frequency of the seismic event with the stress changes that occurred near the tunnel face. Figure 34 compares the total number of seismic events and the maximum deviatoric stress change to the tunnel face chainage. Each parameter has been normalized. Figure 34 shows that the number of seismic events is strongly correlated to the deviatoric stress

Fig. 33. Hoek–Brown failure envelope for Lac du Bonnet granite based on laboratory peak strength (Lab Peak), long-term strength (Lab σ_{cd}) and in situ crack-initiation stress (σ_{ci}) from the microseismic monitoring.

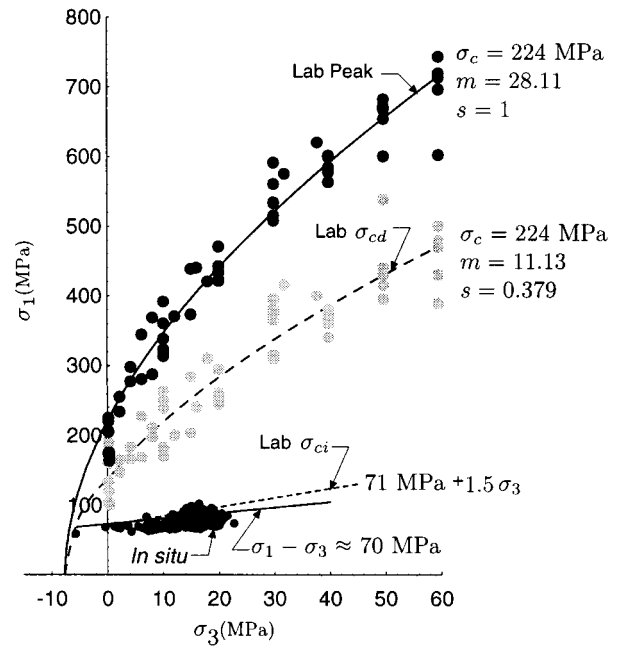
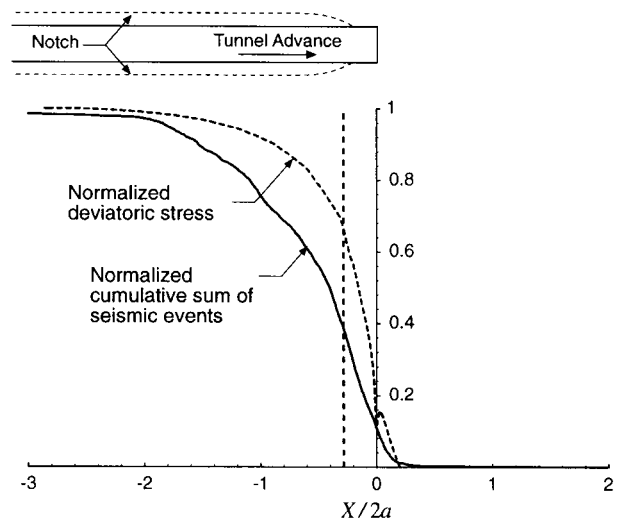
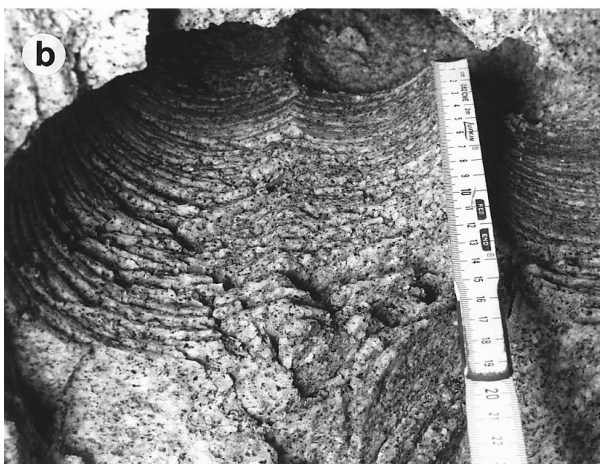
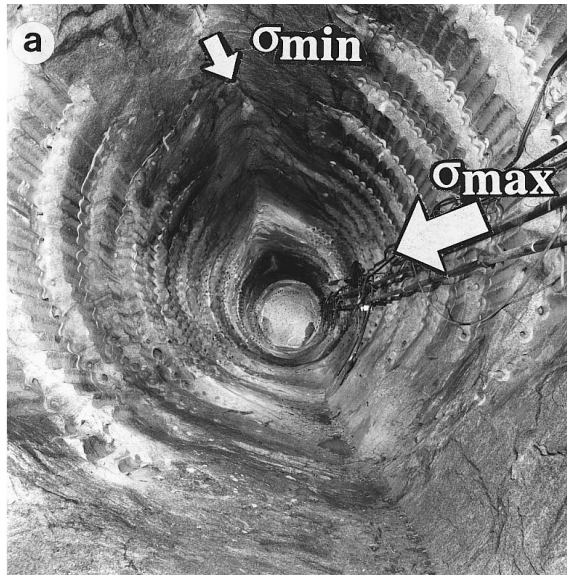


Fig. 34. Comparison of the normalized maximum deviatoric stress with the normalized cumulative microseismic events, in the region of the notch. The face position X has been normalized to the tunnel diameter $2a$.



changes and that both the deviatoric stress changes and the seismic events are completed within two tunnel diameters of the tunnel face. Martin et al. (1995) found that the rate of microseismic activity and the development of the notch shown in Fig. 24 also correlated with the deviatoric stress changes. They further noted that the shape of the notch was very similar to the pattern of microseismic events that occurred before the notch started to develop, indicating that the notch would form in the pre-damaged rock.

Fig. 35. The Mine-by test tunnel showing the well-developed notch and typical slabs that formed the notch. (a) View of completed test tunnel. (b) Thin slabs from the roof of the test tunnel.

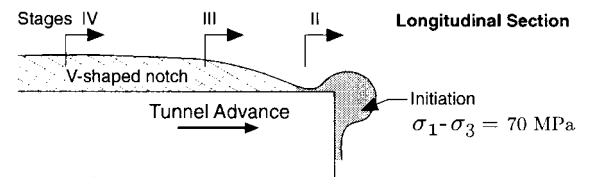


Failure process observations

The method used for the excavation of the test tunnel provided unique opportunities to observe and measure the development of the notch in the roof. Special care was taken to ensure that the wire mesh in the roof which was used for operational safety, i.e., to collect the “loose” from the roof, did not inhibit the development of the notch. This meant that periodically the wire mesh had to be removed and the loose cleaned up. At the end of the tunnel excavation, the wire mesh and the tunnel muck on the floor were removed. The consistency of the tunnel notch in both the roof and floor can be seen in Fig. 35a. It is important to note that, although the failure process in brittle rock is violent as a result of the sudden release of strain energy, once plane-strain conditions are achieved the new tunnel geometry is stable. The observations made during the notch formation are summarized in Fig. 36 and a brief description of the failure process follows.

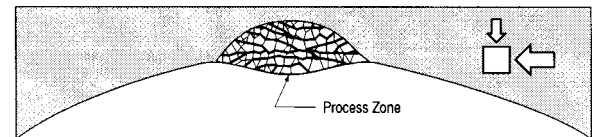
The slabbing in the roof and floor of the Mine-by tunnel was observed to start at about 1 m from the face, immediately after each excavation round was taken, and failure progressed

Fig. 36. Illustration of the major processes involved in the initiation, development, and stabilization of the V-shaped notch.



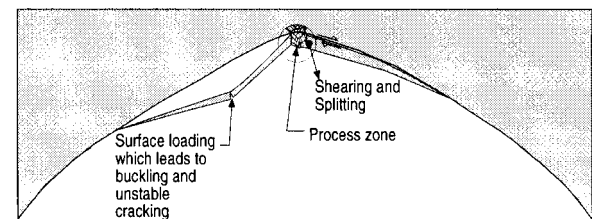
Stage I - Damage Initiation

Cracking initiates ahead of the tunnel face in the region defined by the deviatoric stress exceeding a critical value.



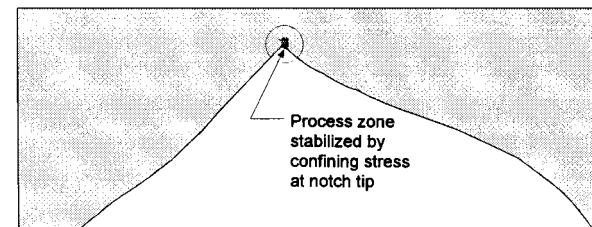
Stage II - Dilation

Critically oriented flaws are exploited in the zone of maximum tangential stress. This process initiates at the boundary of the tunnel. Shearing and crushing occur in a very narrow process zone about 5 - 10 cm wide. Extensive dilation, at the grain-size scale, occurs in this process zone.



Stage III - Slabbing & Spalling

Development of the process zone leads to the formation of thin slabs. These thin slabs form by (1) shearing, (2) splitting, and (3) buckling. The thickness of the slabs varies from 1 to 5 cm. The thickest slabs form as the notch reaches its maximum size. Near the notch tip the slabs are curved.



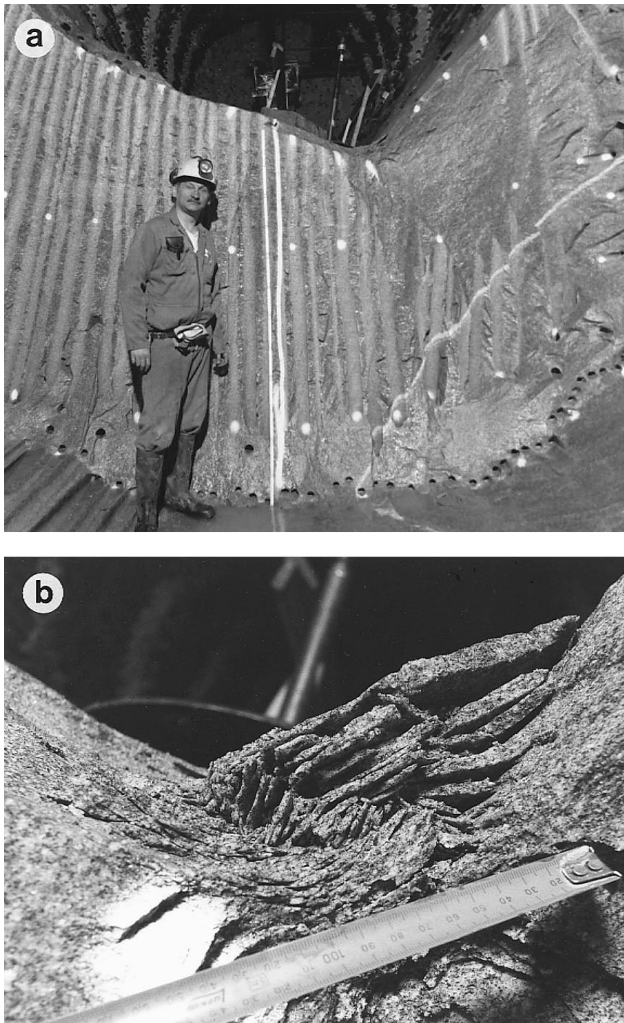
Stage IV - Stabilization

The development of the notch stops when the notch geometry provides sufficient confinement to stabilize the process zone at the notch tip. This usually means there is a slight “tear-drop” like curvature to the notch shape.

as the tunnel face was advanced. The thickness of the spalling slabs which created the notch varied from a few millimetres to ≤ 100 mm, and there did not appear to be any preferred side of slabbing, i.e., the slabs formed on both sides of the notch. Regardless of the process causing the notch development, the orientation of the final notch was consistent with the $11\text{--}14^\circ$ plunge of σ_1 over the entire 46 m length of the test tunnel (see Fig. 26).

The notch development is a three-dimensional process. As shown in Fig. 36, the steps involved in the formation of the notch are (I) damage initiation, i.e., microcracking of the rock ahead of the tunnel face; (II) visible crushing in a very narrow, 5–10 cm wide, process zone on the tunnel periphery, approximately 0.5–1 m back from the tunnel face where the maximum tangential stress exceeds the strength of the damaged rock; dilation and small-scale flaking in this process zone result in the formation of thin

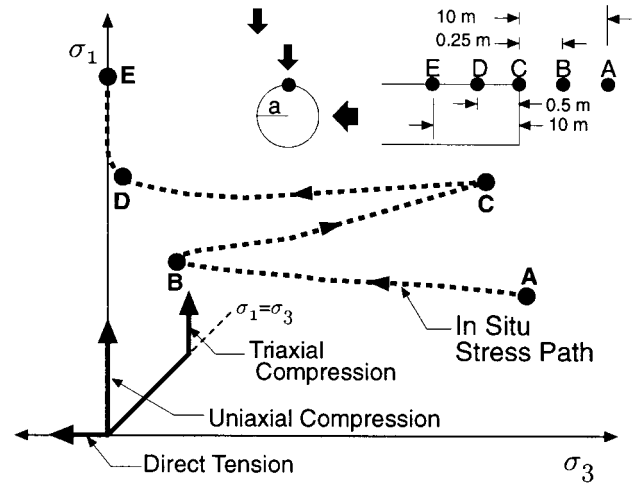
Fig. 37. Shape of the notch after stability is achieved (stage IV in Fig. 36). Note that at the notch tip the failure mechanisms in the process zone are visible. If this failed material were removed, a slab will form on the flank of the notch. (a) Notch shape. (b) Process zone at the notch tip.



slabs that are typically as thick as the grain size of the granite (2–5 mm); (III) formation, in an unstable manner, of larger thin slabs on the flanks of the notch as the process zone develops; and (IV) stabilization of the process zone when the notch geometry provides sufficient confinement to stabilize the process zone at the notch tip (Fig. 37b). This occurs when the geometry takes on a tear-drop like shape (Fig. 37a). The tear-drop like geometry of the notch re-orientes the principal stresses locally and results in high values of σ_1 and associated high confinement.

In summary the brittle failure process is characterized by thin slabs spalling off the excavation boundary. These slabs, where held in place by the wire mesh, resemble a “deck of cards” with essentially no cohesion between the slabs. Once the wire mesh is removed, these slabs fall under gravity loading. Near the tunnel face where the wire mesh was not installed, the slabs fall as they form. The notch geometry expresses the region around the tunnel where the cohesion loss, caused by the

Fig. 38. Stress path for laboratory tests compared with the stress path experienced by the rock mass in the roof of the test tunnel.



slabbing, is 100%. Martin et al. (1997) showed that the rock mass immediately surrounding the notch tip also contains thin slabs but there the cohesion-loss process is not complete and hence the slabs are still attached.

In the next section the failure process is tracked from its initiation (step I in Fig. 36) through to the plane-strain conditions where stability is achieved (step IV in Fig. 36).

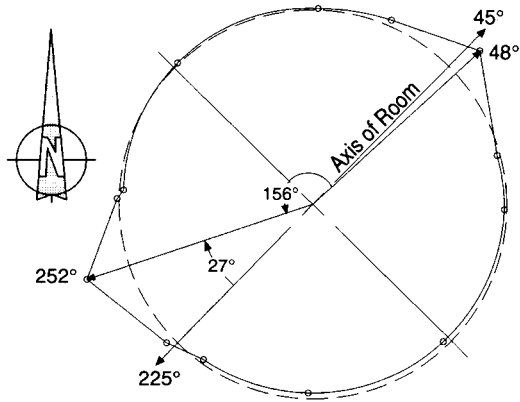
Stress path and rock mass strength

When considering the ultimate strength of a material it is important to know the loading path that has been used to measure the strength, e.g., rock is much weaker in tension than in compression. In the laboratory, tests are routinely performed to obtain the tensile strength, unconfined compressive strength, and triaxial strength. In all these tests the loading path is monotonically increasing or decreasing. However, in situ the loading path around a tunnel is more complex, involving stress increase, decrease, and rotation in the regions close to the advancing excavation face. The actual stress path experienced by the rock mass in the roof of the test tunnel can be estimated by using three-dimensional linear elastic stress analyses and plotting the results in $\sigma_1 - \sigma_3$ stress space (Fig. 38).

Five key reference points (A, B, C, D, E) were chosen, relative to the tunnel face, to aid in tracking the stress path as the tunnel approaches and passes the volume of rock that is being monitored. For example, in every analysis, the reference point starts 10 m ahead of the tunnel and is referred to as the far-field (point A in Fig. 38), and its stress path is followed until the tunnel has passed the reference point by 10 m (point E in Fig. 38) corresponding to approximately plane-strain conditions. Using this approach the stress path followed by reference point A can be tracked.

A numerical model that properly simulates the brittle-failure process is required to accurately quantify the stress redistribution that occurs around a tunnel in yielding-failing ground. However, in three dimensions such models become very complex and frequently require large amounts of computer run time. In addition, to the author’s knowledge, constitutive models that adequately capture the brittle-failure process described in Fig. 36 are not available. Hence, three-dimensional linear elastic

Fig. 39. Asymmetric failure zone in a 1.24 m diameter vertical borehole.



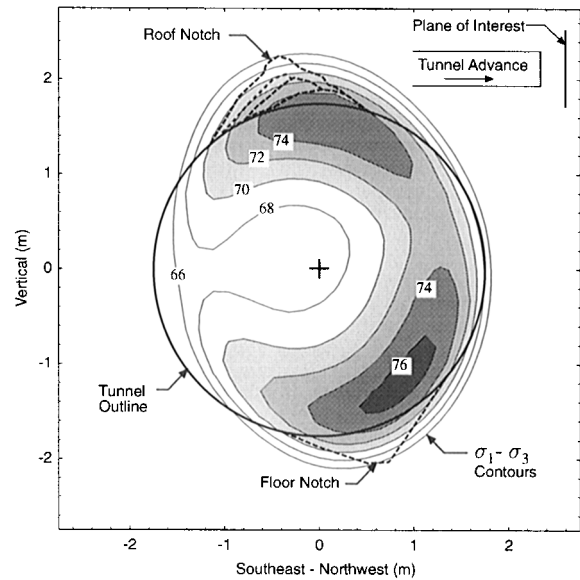
stress analyses for a cylindrical tunnel with a flat face are used to examine the loading path around the Mine-by test tunnel. Such analyses are only valid to the “point” where the rock mass behaviour becomes nonelastic. In the section Initiation of the cohesion-loss process, it was established that this point is approximately coincident with the tunnel face. Thus the stress magnitudes calculated for the loading path inside the tunnel and close to the tunnel boundary can only be viewed as approximate magnitudes, whereas the magnitudes ahead of the tunnel face are considered more representative of the actual rock mass response. In this section, elastic analyses are used to estimate the in situ strength of the rock mass around the Mine-by test tunnel. The in situ strength is approximated by considering the effect of crack-induced damage on the cohesion component of rock strength, from initiation of damage through to the development of the “notch.”

Preconditioning damage ahead of the tunnel face

One of the observations made during the excavation of circular openings at the 420 Level of URL was that the failed zones did not form directly opposite each other, i.e., the zones were located asymmetrically around the opening. Two-dimensional elastic theory would suggest that, for the condition of anisotropic far-field stresses, the failed zones should be symmetric, i.e., diametrically opposite each other, if the failure initiated on the perimeter of the circular openings at the maximum tangential stress concentrations. Read (1994) examined the deviatoric stresses ahead of a circular tunnel, using a three-dimensional elastic stress analysis. He showed that deviatoric stresses ahead of an opening, advanced parallel to one of the principal stresses, were symmetric, suggesting that if the failure initiated ahead of the opening face at the maximum deviatoric stress concentrations, the position of the failure would also be symmetric. However, if the opening orientation is not parallel to one of the principal stresses, then the deviatoric stresses ahead of the tunnel face are asymmetric.

Read et al. (1995) found that the failure zones of a 1.24 m diameter borehole drilled from the floor of Room 405 were located at azimuth 48° and 252°, which are only 157° apart instead of the 180° that one would expect if the tangential stress concentrations were solely responsible for causing the failure (Fig. 39). They showed that the asymmetry in the failure pattern which was observed in the borehole correlated to

Fig. 40. Maximum deviatoric stress on a plane located 0.5 m ahead of the tunnel face.



the asymmetry in the pattern of deviatoric stress magnitudes ahead of the advancing borehole face. Read et al. (1995) postulated that, because the deviatoric stresses exceeded 70 MPa, damage was occurring ahead of the advancing borehole and this asymmetric damage pattern accounted for the asymmetric breakouts. They tested this theory by drilling a 600 mm diameter borehole about 3 m away from the location of the 1.24 m diameter borehole but in the direction of σ_3 . For this orientation, the borehole failure pattern was symmetric.

In the section Far-field stress state, it was pointed out that the Mine-by test tunnel was misaligned to σ_2 by about 10°. As a consequence the stresses ahead of the test tunnel are distributed asymmetrically with respect to the tunnel axis. A series of three-dimensional elastic stress analyses was carried out to inspect the stresses ahead of the test tunnel. Figure 40 shows the maximum deviatoric stress pattern on a plane located 0.5 m ahead of the tunnel face. Figure 41 shows the σ_3 contours on the same plane. Note that the shapes of the two stress patterns are quite different. Shown in Fig. 40 is the outline of the notch in the roof and floor. The roof notch outline also contains the development of the notch as measured at one of the monitoring sections. Figure 40 shows that the 70 MPa contour in the roof nearly reaches the notch tip and that the first part of the notch that forms in the roof is in the region where the deviatoric stresses are a maximum (≈ 75 MPa) and hence the damage should be the greatest. It is also important to note that the maximum radial distance of the damage stress is not the same in the roof and the floor. The damage is greatest in the roof. Comparing Figs. 40 and 41 it also appears that the low values of confining stress in the roof may be a contributing factor to the greater damage in the roof compared with that in the floor.

Figure 28 shows the microseismic activity that occurred ahead of the test tunnel face. If the deviatoric stresses are causing the microseismic activity, then there should be a relationship between the microseismic pattern and deviatoric stress pattern. Figure 42 shows the microseismic events that were recorded in the the volume of rock between 0.25 and 0.75 m

Fig. 41. Contours of σ_3 on a plane located 0.5 m ahead of the tunnel face. The grey area corresponds to the region where $\sigma_1 - \sigma_3 \geq 70$ MPa.

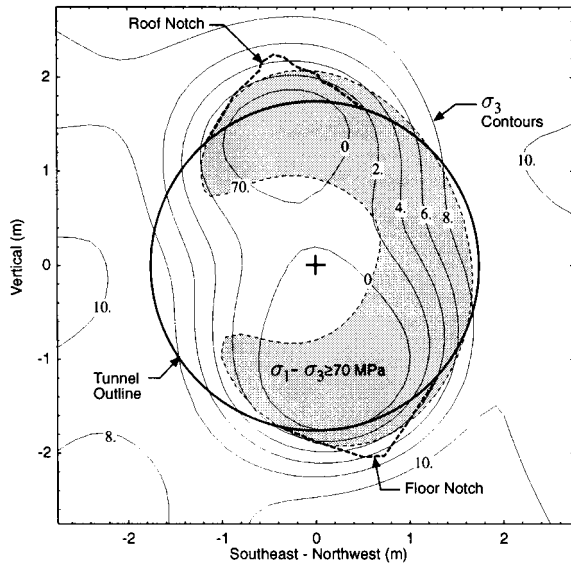
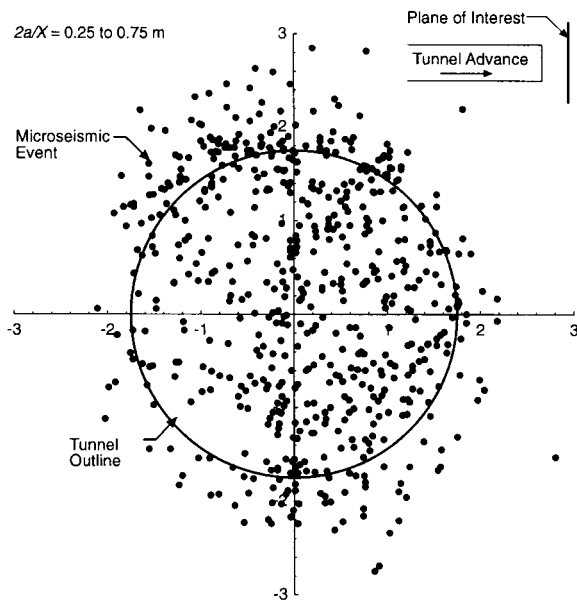


Fig. 42. Location of microseismic events in a volume of rock located 0.25–0.75 m ahead of the test tunnel face.



ahead of the tunnel face. The density of the seismic events is compared with the deviatoric stress pattern in Fig. 43, showing that the asymmetric pattern in the deviatoric stresses is also present in the pattern of microseismic events. Also, note that the largest concentration of microseismic events in the roof correlates with the region of maximum deviatoric stress and low confining stress. It is important to realize that this microseismic activity, i.e., damage, is occurring ahead of the tunnel and that the notch will eventually form in this damaged region.

Crack extension during unloading

The preceding discussion noted that the microseismic events were concentrated in the region that combined deviatoric

Fig. 43. Contours of seismic event density and maximum deviatoric stress on a plane located 0.5 m ahead of the tunnel face.

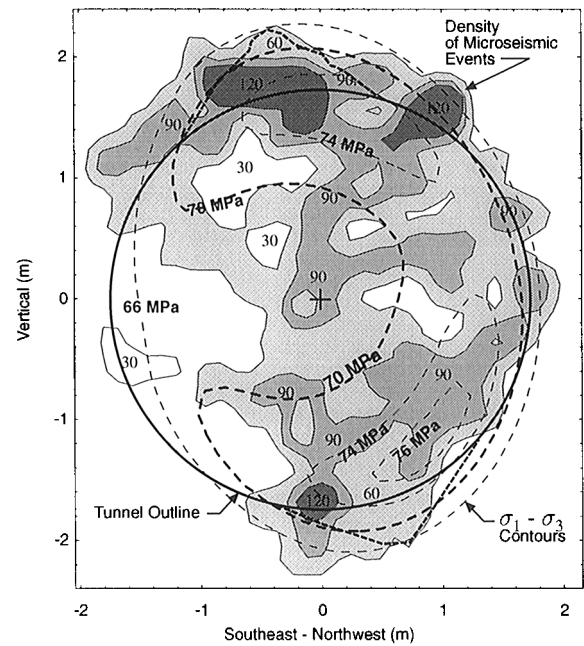
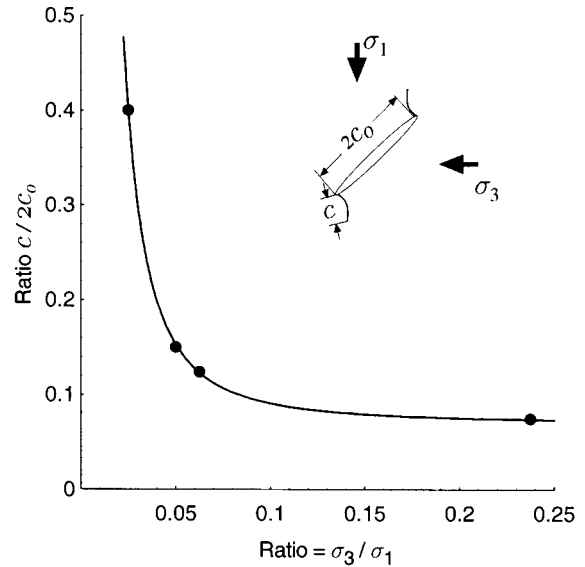
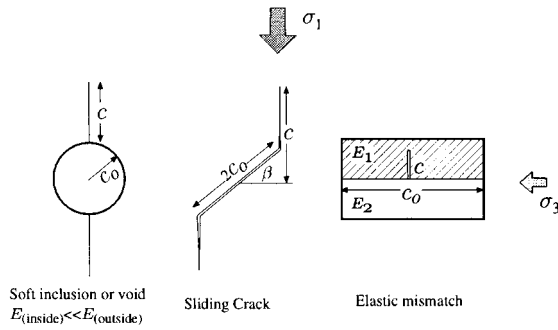


Fig. 44. Relationship between crack propagation and the ratio σ_3/σ_1 . Data from Hoek (1965).



stresses which exceeded the crack-initiation stress and low confining stresses. In the section Initiation of the cohesion-loss process, it was shown that the in situ crack initiation could be predicted using [16]. However, the in situ information does not provide any method for estimating the length of the crack extension once the cracks initiate. Hoek (1965) carried out a series of tests on plates of glass to examine the relationship between crack growth and the ratio σ_3/σ_1 (Fig. 44). Figure 44 implies that as the ratio σ_3/σ_1 approaches zero the lengths of the wing cracks are infinite. This can only occur if the crack-opening force is held constant. The inclined surface in Hoek’s experiment serves as a crack-opening force to propagate mode

Fig. 45. Models used to develop Fig. 46.



I cracks. Usually the crack-opening force will be associated with a finite stiffness, and hence the crack-opening force will decrease as the crack lengthens. Thus, the length of the crack will be finite.

Kemeny and Cook (1991) investigated the propagation of mode I cracks in a compressive stress field. Three of the crack-growth models investigated by Kemeny and Cook were (1) cracks around a cylindrical pore (or soft inclusion); (2) cracks resulting from sliding along existing discontinuities; and (3) cracks caused by differential strain at the interface of mismatched elastic materials (Fig. 45). Using linear elastic fracture mechanics, the fracture will propagate when the stress intensity factor (K_I) exceeds the fracture toughness (K_{Ic}). For example, the stress intensity factor for the sliding-crack model when $c \gg c_0$ is given by Kemeny and Cook (1991) as

$$[17] \quad K_I = \frac{2c_0 \tau \cos \beta}{(\pi c)^{1/2}} - \sigma_3 (\pi c)^{1/2}$$

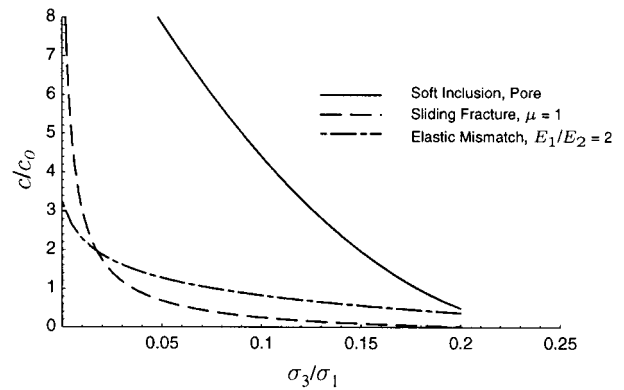
where

$$\tau = \frac{1}{2} [(\sigma_1 - \sigma_3) \sin 2\beta - \mu(\sigma_1 + \sigma_3 + (\sigma_1 - \sigma_3) \cos 2\beta)]$$

and β is the inclination of the crack to σ_3 . Equation [17] can be used to determine the length the crack will propagate as a function of σ_3/σ_1 . Figure 46 shows the results for all three models using $K_{Ic} = 1.5 \text{ MPa(m)}^{1/2}$, for Lac du Bonnet granite (Martin 1993) and keeping $\sigma_1 = 50 \text{ MPa}$. The sliding-crack model and the elastic mismatch models show a relationship between crack extension and the ratio σ_3/σ_1 similar to what Hoek (1965) measured in the laboratory, with the sliding-crack model providing the best agreement with Hoek's data. However, unlike Hoek's data the sliding-crack model indicates that the crack length is finite when $\sigma_3/\sigma_1 \rightarrow 0$. The pore model, although exhibiting the largest crack, is an unlikely model for Lac du Bonnet granite because of the low porosity in situ, i.e., $<0.1\%$.

Both the experimental data and the stress intensity factor approach suggest that, as a closed fracture is unloaded, the tips of the crack will extend in the direction of the maximum applied load. Mismatched elastic properties can also give rise to crack extension. As given by [11], an increase in crack length above the average background crack length leads to a reduction in strength. To describe the results from Figs. 44 and 46, a general equation relating crack extension to the ratio σ_3/σ_1 can be expressed as

Fig. 46. Length of cracks as a function of the ratio σ_3/σ_1 ratio based on K_{Ic} for the models given in Fig. 45.



$$[18] \quad c = A + \frac{B}{\exp\left(\frac{\sigma_3/\sigma_1}{C}\right)}$$

where A , B , and C are curve-fitting parameters. As stated previously the excavation of a tunnel is essentially an unloading process combined with an increase in the tangential stresses. Hence, [18] will be used in the following section to investigate the amount of crack extension and subsequent strength loss as the rock mass around the tunnel is unloaded.

Unloading stress path and rock strength

Three-dimensional elastic analyses were carried out to track the change in rock strength as the rock mass follows the stress path dictated by the tunnel excavation. In carrying out the stress analyses, special care was taken to avoid the problem of the stress singularity at the corner of the tunnel face. This problem was considered by increasing the number of elements in this region and also by obtaining the stress information at a distance of 50 mm from the tunnel wall. Sensitivity analyses were carried out and the high stress magnitudes caused at the corner drop dramatically at a distance of 50 mm. A consequence of being 50 mm from the tunnel wall is that once inside the tunnel the confining stress is usually greater than zero. However, this does not impact on the analyses or conclusions. Only those analyses in the notch regions in the roof and the floor are considered, as it is only in those areas that failure has been measured. Equation [11] is used to determine the strength of the rock mass, with the crack length in [11] adjusted using [18] for each σ_3/σ_1 . This is plotted as open circles and called the unloading strength. It is only plotted for points (σ_3/σ_1) corresponding to the shown stress path.

Figure 47a presents the stress path followed by a point in the roof of the tunnel located about 50 mm from the tunnel perimeter, and Fig. 47b is the stress path followed by a point in the roof of the tunnel located about 500 mm from the tunnel perimeter. These results show that near the tunnel perimeter, the stress path exceeds the crack-initiation stress well ahead of the tunnel face, but away from the tunnel perimeter the crack-initiation stress is only exceeded as the plane-strain condition is reached. The analyses of the stress path in the floor produced similar results (Fig. 47c). Additional analyses also showed that at a distance of 1 m beyond the tunnel wall the crack-initiation stress is not reached and thus the rock is undamaged.

From the laboratory tests in section 2 two key stress levels were identified in the failure process, namely crack initiation and long-term strength. The corresponding stress levels along the stress path in Fig. 47a for undamaged granite would be the crack-initiation stress (near point B) and long-term strength (point D). The crack-initiation stress in both the laboratory case and in situ occurs at about 70–75 MPa. Spalling was first observed in the test tunnel roof at about 0.5 m behind the tunnel face (point D in Fig. 47a). At this point, σ_1 reaches about 100–120 MPa (0.5 to 0.6 σ_c). In the laboratory, this long-term strength was approximately 160 MPa (0.7 to 0.8 σ_c). This decreased in situ strength is attributed to the difference in the loading path used to obtain the laboratory strength and the in situ unloading path experienced by the rock mass around the test tunnel.

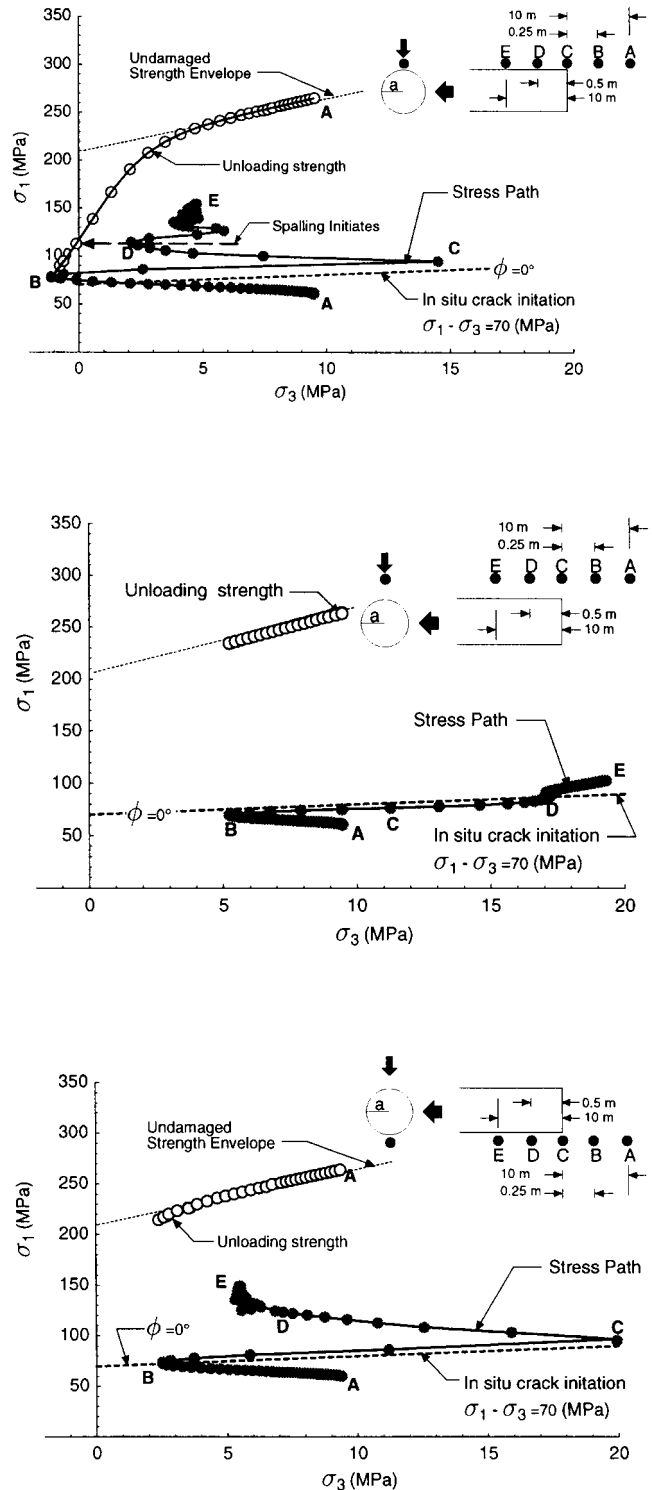
As the rock mass is unloaded the deviatoric stresses exceed the crack-initiation stress (Fig. 47a). However, because $\sigma_3/\sigma_1 \rightarrow 0$, cracks are also extending. By combining [18] and [11] the analyses indicate the rock strength decreases. Interestingly, the strength has decreased to about 100 MPa by point B in Fig. 47a. Once this cohesive strength component is lost it cannot be regained and in this way is path dependent. Although the roof rock mass strength has been decreased, the rock mass in the floor at the same distance from the tunnel wall, i.e., 50 mm, does not experience the same amount of strength decrease because the unloading has not been as severe, i.e., essentially no damage. It is recognized that the actual amount of strength reduction is a function of the model developed for [18]. Nonetheless, any model will show a greater strength loss in the roof than in the floor because of the asymmetry of the stress magnitudes. It should also be realized there will be damage in the floor very close to the tunnel wall because there the rock mass has been completely unloaded. These analyses merely point out that the depth of damage should be greatest in the roof, and this is supported by observations and measurements (see Fig. 24). Initially, it was thought that the confining stress caused by the tunnel muck in the floor was the main reason for the reduced damage in the floor. Although there is evidence to suggest that the confining pressure supplied by tunnel muck did contribute to the reduced damage, these analyses suggest that the loading path is the main reason for this reduced damage.

Stress rotation

Wu and Pollard (1995) conducted tensile tests on a brittle material to investigate the influence of the orientation of existing cracks on crack growth in tension. By rotating the applied tensile stress relative to the orientation of the existing cracks they demonstrated that the existing cracks influenced the growth of new cracks. They also demonstrated that by simply keeping the stress constant but rotating its direction they could generate crack patterns in different directions. At rotation angles from about 0 to 45° they showed that new cracks tended to grow from the tips of existing cracks, i.e., the existing cracks grew longer without an increase in stress. Using the energy approach of Griffith (1921), Orowan (1949) has shown that the tensile strength (σ_t) of a material is controlled by the crack length in the material and is given by

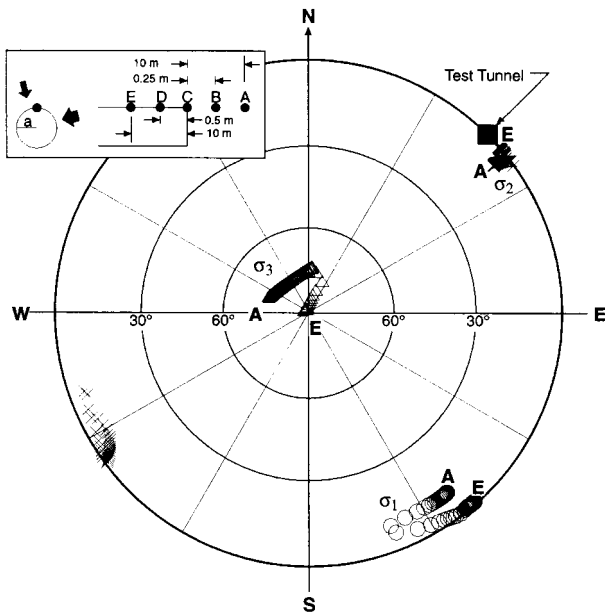
$$[19] \quad \sigma_t = \frac{K_{Ic}}{(\pi c)^{1/2}}$$

Fig. 47. Stress path for a point located 50 mm (a) and 500 mm (b) from the tunnel wall at the maximum compressive stress concentration in the roof and at 50 mm in the floor (c). The far-field point (A) is located 10 m ahead of the tunnel face, and point E represents plane-strain conditions around the tunnel.



where c is the crack half-length, and K_{Ic} is the mode I fracture toughness. Hence, the material subjected to stress rotation would be weaker than the material loaded without stress rotation,

Fig. 48. Rotation of the principal stresses shown on a lower hemisphere equal-area stereonet. The monitoring point is similar to that shown in Fig. 47a but is located vertically above the centreline of the test tunnel in the roof.



as the latter would have shorter cracks. It is suggested here that crack growth, induced by stress rotation, could also occur in compression loading.

The advance of the tunnel face not only causes the stress tensor to change in magnitude but also causes the stress tensor to rotate. Cracks grow in the plane perpendicular to σ_3 , therefore the rotation of σ_3 represents the rotation of the pole normal to the plane of the crack. Martin (1993) carried out detailed analyses around the tunnel face and concluded that rotation of σ_3 occurs everywhere around the tunnel face. However, it is only in the roof of the test tunnel that the rotation of σ_3 is at a maximum, about 20–30° close to the tunnel perimeter (Fig. 48), and this value decreases to about 5° at 0.5 m from the tunnel perimeter. It is important to note that the out-of-plane rotation is also greatest in the compressive regions around the tunnel. Although the stress rotations around the test tunnel are relatively small, stress rotations >40° have been reported by Kaiser (1994) for a mining environment. Therefore, stress rotation related damage or magnification of damage should be expected around some underground openings.

The stress rotation in Fig. 48 initiates ahead of the tunnel when the stresses are above the crack-initiation stress (as shown in Fig. 47), and the location of this maximum stress rotation region is coincident with the region in the roof of maximum deviatoric stress shown in Fig. 40. Hence, the rock mass strength near the tunnel face may be degraded further by stress rotation. Equation 11 illustrates that any form of crack growth results in a loss of cohesion and a subsequent reduction of the rock mass strength. This form of cohesion loss would be greatest at the tunnel perimeter where the stress rotation and deviatoric stress magnitudes are the greatest.

Summary

The logic described in the preceding discussion requires that the stress magnitudes near the tunnel face are sufficient to exceed the in situ crack-initiation stress. As the face of the tunnel approaches and passes the volume of rock that eventually becomes part of the tunnel surface, the principal stresses associated with this rock will change significantly in both magnitude and direction. Stress concentrations in excess of the crack-initiation stress, occurring at any period in the rock's loading history, will result in a localized increase of damage to the rock and a corresponding loss of cohesion. The degree of damage will be highest at the surface of the opening where confinement is zero and deviatoric stress concentrations are greatest, and this damage will decrease with increasing distance into the rock. Figure 47 suggests that this damage will only occur in the regions where the confining stress is reduced to less than 5 MPa. It is important to note that the cracks causing the damage to the rock mass are very small, with stress drops that are less than those recorded from microseismic events generated by controlled small-scale laboratory shear experiments (McGarr 1994).

It is also clear, from the results in this section and in the section Failure in laboratory compression tests, that a major difference between laboratory tests and in situ conditions is that, although the laboratory strength is estimated by increasing the loads via a simple stress path, the in situ strength is mobilized essentially by unloading the rock mass through a complex stress path. As a result it seems unreasonable to expect the laboratory strength to match the in situ strength.

Predicting the depth of progressive brittle failure

The previous sections showed that the failure process around the test tunnel is three-dimensional involving a complex stress path. Read and Martin (1996) concluded that current continuum and discontinuum models cannot predict the extent and depth of failure because they cannot follow this stress path, i.e., the transitions from the elastic rock mass through to the slabbing process. Efforts are currently underway to establish if newly developed micromechanical models are adequate for this type of problem (Cundall et al. 1996). Although our current continuum models are not suited to capture all aspects of the failure process, two-dimensional analyses can be instructive when guided by our understanding of the failure process. Also, there is still a practical need to determine if continuum models can be used to estimate the maximum depth of progressive brittle failure and damage, as these are of interest for support design. In the following sections, two-dimensional analyses are used to estimate the failure around the test tunnel. It is recognized that the rock mass never "sees" a circular tunnel in plane-strain conditions and hence the results from such two-dimensional plane-strain analyses must be considered as illustrative only.

A widely used rock mechanics strength criterion is the empirical Hoek–Brown failure criterion (Hoek and Brown 1980a, 1988) given by

$$[20] \quad \sigma_1 = \sigma_3 + (m\sigma_c\sigma_3 + s\sigma_c^2)^{1/2}$$

where σ_c is the laboratory uniaxial compressive strength, and m and s are empirical parameters. The values of m and s are in

Table 1. Summary of the laboratory properties for Lac du Bonnet granite.

Parameter	Damage initiation (σ_{ci})	Long-term strength (σ_{cd})
Hoek–Brown		
σ_c (MPa)	224	224
m	0.1	11.13
s	0.098	0.379
Mohr–Coulomb		
Cohesion (MPa)	35	28.4
ϕ (°)	0	47

a general sense related to the angle of internal friction of the rock mass and the cohesion or interlocking of the rock mass, respectively. At the boundary of a tunnel where $\sigma_3 = 0$, [20] reduces to

$$[21] \quad \sigma_{1f} = (s\sigma_c^2)^{1/2}$$

Because of the square-root term in [21], a rock mass with a cohesive strength of 50% of the cohesion measured in the laboratory would have an equivalent s value of 0.25. Table 1 gives the Hoek–Brown and Mohr–Coulomb parameters for Lac du Bonnet granite. These parameters are used in the analyses in this section.

Iterative elastic analyses

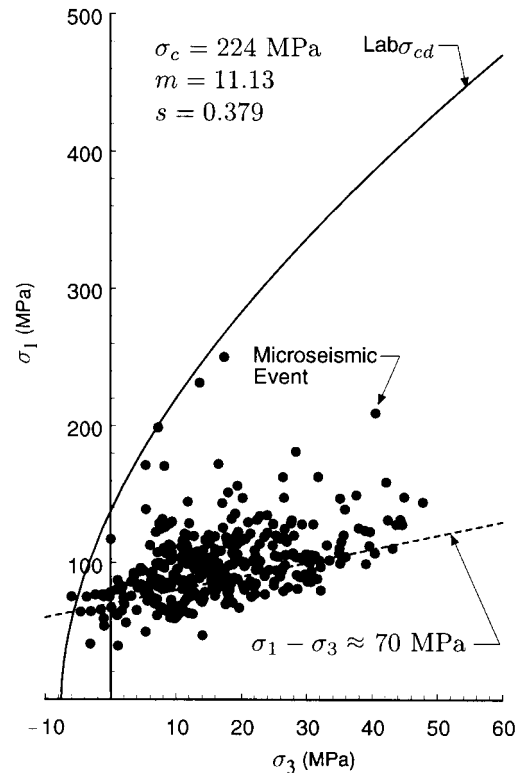
The Mine-by test tunnel offers an ideal case for back analyses: the stress state is well constrained; the extent of failure is well defined; and the rock mass, except for the notch and damaged region in close proximity, is essentially elastic. The maximum tangential stress (σ_θ) at the boundary of a circular tunnel, for two-dimensional plane-strain conditions, is given by the well-known Kirsch solution as

$$[22] \quad \sigma_\theta = 3\sigma_1 - \sigma_3$$

where σ_1 and σ_3 represent the far-field in situ stresses in the plane of the section. Comparing the maximum tangential stress, given by [22], to the peak unconfined strength of the undamaged Lac du Bonnet granite indicates that the tunnel should be stable, e.g., $\sigma_\theta = 167$ MPa compared with $\sigma_c = 224$ MPa. In the section Failure in laboratory compression tests, it was shown that the long-term strength of the laboratory samples is given by the stress level at which the cohesion strength component is exceeded, and this can be approximated by 0.7 to 0.8 σ_c . Using a long-term strength of 160 MPa ($\approx 0.7 \times 225$ MPa), very minor spalling of the tunnel surface might be anticipated as σ_θ decreases rapidly away from the tunnel perimeter.

In the section Initiation of the cohesion-loss process, the microseismic events were used to establish when the cohesion-loss process initiated. The same approach was used to establish the stresses at the microseismic events associated with the slabbing in the notch. Three-dimensional elastic analyses that included the notch geometry were carried out for round 17 (see Fig. 27). The results are shown in Fig. 49 along with the long-term strength envelope based on laboratory results (see Fig. 33). The elastic stresses represent the maximum stress possible, as plastic straining close to the notch would result in stress redistribution and lower stresses. It is clear from Fig. 49 that the notch develops, i.e., slabbing occurs, at stresses well below the long-term strength.

Fig. 49. Stresses computed for each microseismic event recorded for Round 17 associated with the formation of the notch (see Fig. 27 for distribution of microseismic events).



Samples were obtained from a borehole drilled down the centre of the test tunnel and subjected to laboratory tests. Martin and Stimpson (1994) have shown that those samples were highly disturbed (microcracked) by the sampling process because of the high in situ stresses. Hence, the properties of those samples are not representative of the undamaged in situ rock mass. Martin and Stimpson noted that the sampling damage-process was also one of cohesion loss and resulted in the unconfined cohesive strength being reduced to 114 MPa, i.e., $s = 0.26$ for the long-term strength in Table 1. It is suggested that the sampling process has subjected these samples to a stress path that is similar to that experienced by the rock mass surrounding the test tunnel, and therefore $s = 0.26$ is representative of the strength of the damaged rock near the wall of the test tunnel. This is also in keeping with the results in the section entitled Unloading stress path and rock strength, which showed that failure occurred around the test tunnel when σ_θ reached a value between 100 and 120 MPa.

Two-dimensional elastic analyses were carried out using the boundary element program Examine^{2D} (Curran and Corkum 1995a) to simulate the progressive nature of the failure process. Initially the analysis starts with a circular opening and a factor of safety, or strength factor in Examine^{2D}, is calculated using the Hoek–Brown parameters for the long-term strength, with $s = 0.25$. The analyses indicate that for the stress conditions for the 420 Level failure will form as a thin skin in the floor and roof of the test tunnel (Fig. 50). The progressive nature of the failure process was approximated by removing this failed material, i.e., where the strength factor is less than one, and repeating the analysis. This is similar to the slabbing process observed during

Fig. 50. The depth of failure for the Mine-by test tunnel predicted using an elastic analysis and Hoek–Brown parameter for the long-term strength with $s = 0.25$.

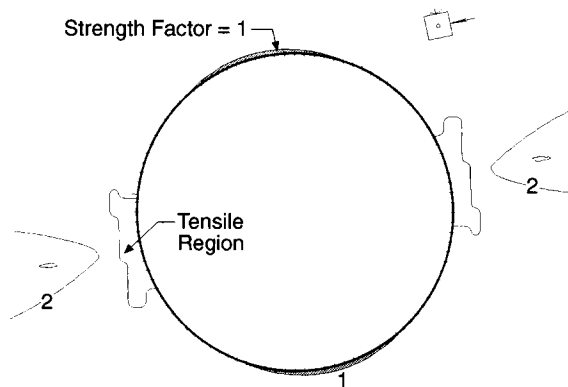
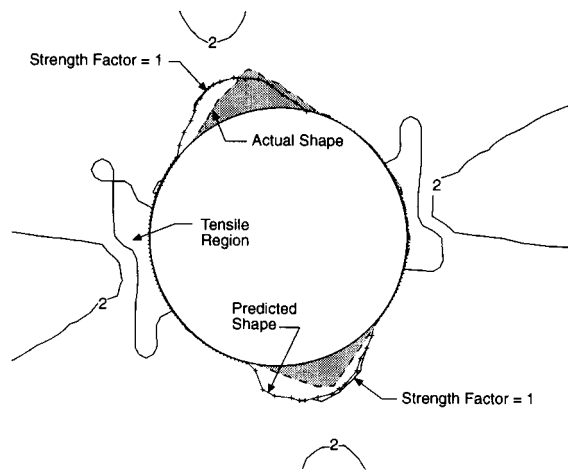


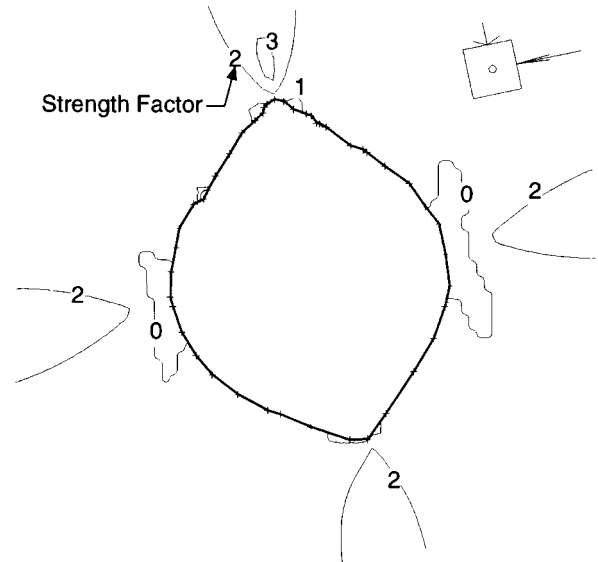
Fig. 51. Shape of the notch, after 49 steps, for an elastic model with an iterative slab removal scheme compared with the measured shape. The notch, at this stage, is unstable and more slabs must be removed.



the excavation of the test tunnel. After 17 analyses the notch is well defined (Fig. 51). However, the analyses indicate that failure is still occurring and therefore the notch will continue to grow beyond that shown in Fig. 51. These analyses were carried out by manually adjusting the tunnel boundary to remove the failed material. Like all numerical analyses, the irregularities of the tunnel boundary in the notch region can significantly affect the stress concentrations and hence the depth of failure. In an effort to remove the effect of these stress concentrations Read (1994) developed an automated procedure in the finite difference program FLAC (Cundall and Board 1988) to simulate the failure process by the removal of material and subsequent smoothing of the mesh. Using this technique Read found that the depth of failure extended in his model to one radius beyond the tunnel perimeter. This is also in keeping with the findings of Zheng et al. (1989), who modelled borehole breakouts using a boundary element technique and a similar element removal technique to represent progressive failure.

The numerical two-dimensional models that utilized an iterative slab removal scheme to simulate progressive failure overpredicted

Fig. 52. Computed strength factor for the actual shape of the test tunnel. Note the high strength factors at the notch tip caused by a rapid increase in confining stress around the notch.



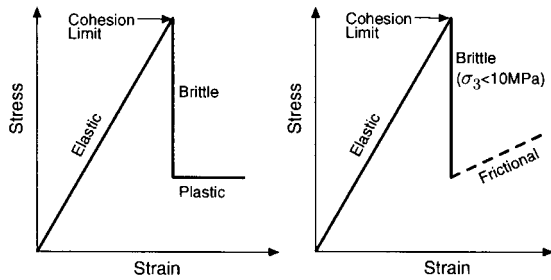
the depth of failure by a factor of 2 to 3. It is suggested that the main reason for the overprediction is related to the shape of the modelled notch. Because the notch is modelled by removal of a thin slab of material that extends along the tunnel perimeter, the notch shape becomes quite rounded compared to its actual shape (see Fig. 51). Thus the geometry used in the computer simulations promotes failure while the actual “pointed” shape inhibits the failure process (Fig. 37). The reduction in the radius of curvature of the pointed notch promotes the rapid increase in σ_3 at the notch tip which increases the strength factor immediately beyond the notch tip (Fig. 52). Another equally important aspect of the pointed notch tip is its ability to inhibit the dilation process associated with brittle failure and hence also increase confinement (see Fig. 37). Thus the notch shape is critical. The mismatch between the iterative elastic analyses and reality suggests that the progressive failure process is not well captured by this approach.

Strain-softening approach

Traditionally, the failure of brittle rocks is simulated assuming elastic–brittle–plastic behaviour, similar to that illustrated in Fig. 53. The hybrid boundary finite element program PHASES (Carvalho et al. 1991) was specifically developed for this type of problem. The program automatically generates a graded finite element mesh around the opening and the graphical pre- and post-processor interface provides a user-friendly environment to conduct analyses. Analyses of the Mine-by test tunnel were carried out using PHASES and a strain-softening model with the long-term strength values in Table 1 and residual values of m and s as 1 and 0.01, respectively, as suggested by (Hoek et al. 1995), to represent the rock spalling and falling away from the roof of the excavation. Figure 54 shows that this approach significantly underpredicts the depth of the notch.

In the section Failure in laboratory compression tests, it was shown that, in the brittle-failure process, friction is mobilized after a significant loss of cohesion (see Fig. 13). Figure 55 illustrates this concept in terms of a Mohr stress diagram. A

Fig. 53. Illustration of the elastic–brittle–plastic behaviour assumed in traditional strain-softening models compared with the proposed cohesive–brittle–frictional (CBF) model.



cohesive– brittle–frictional (CBF) constitutive model is proposed that simulates the brittle-failure process illustrated in Fig. 55. In this model yielding occurs when the constant-deviatoric-stress criterion for damage initiation, given by $\sigma_1 - \sigma_3 = 70 \text{ MPa}$, is exceeded. Once yielding initiates there is a drop in cohesion and friction is mobilized. The residual values for cohesion of 7.46 MPa and $\phi = 47^\circ$ for Lac du Bonnet granite, reported by Martin and Chandler (1994), are used in the following analyses. These values were determined immediately after the rapid loss of cohesion (see Fig. 12) and when combined with the constant-deviatoric-stress criterion provide the failure envelope illustrated in Fig. 55. The largest reduction in cohesion occurs where confining stresses are low.

Figure 56 shows the results from the numerical program PHASES using the the CBF strain-softening model. Also shown in Fig. 56 is the actual notch shape. Although the distribution of yield points in Fig. 56 does resemble the distribution of microseismic events recorded near the face of the test tunnel as the notch forms (see the end view in Fig. 27), this model does not capture the shape of the notch. Nonetheless this approach may provide more realistic stresses and deformations within the yielding rock and hence be more suitable for estimating rock support requirements.

Constant-deviatoric-stress criterion

The microseismic studies described in the section Initiation of the cohesion-loss process showed that [16] can be used to define the initiation of damage ahead of the tunnel face. Here [16] will also be used to determine the potential region of damage around the test tunnel under plane-strain conditions. Figure 57 shows the contours around the test tunnel, from elastic analyses, for $\sigma_1 - \sigma_3$ of 65, 70, 75, and 80 MPa. Although the lateral extent of the contours varies significantly, the radial extent of damage is well constrained, particularly in the vicinity of the notch. Also plotted in Fig. 57 is the surveyed shape of notch near round 17 (see Fig. 23), and the microseismic events recorded within a 1 m thick slice around the test tunnel, i.e., $\pm 0.5 \text{ m}$ of the surveyed section. It is obvious that the constant-deviatoric-stress criterion does not define the shape of the notch, but it does provide a reasonable estimate of the maximum depth of damage (the region containing the microseismic events) and the depth of notch development in the roof. As mentioned previously, the development of the notch in the floor was influenced by both the confining stress provided by the tunnel muck and the different stress path in the floor. Although the constant-deviatoric-stress criterion is a gross simplification, it captures a fundamental characteristic of brittle

Fig. 54. Damage, predicted by the numerical program PHASES, around the Mine-by test tunnel using an elastic–brittle–plastic strain-softening constitutive model.

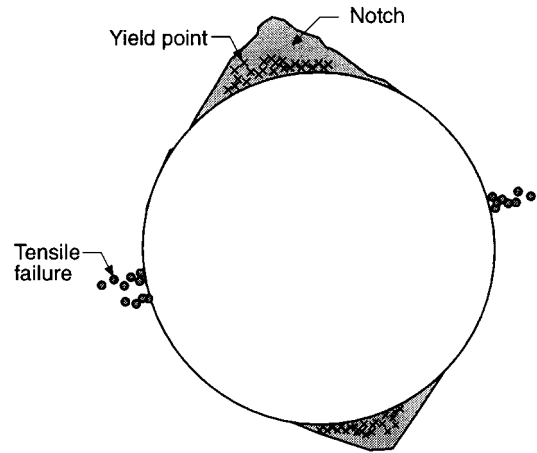
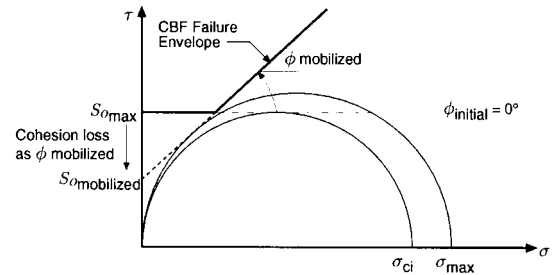


Fig. 55. Illustration of cohesion loss and mobilization of friction in terms of Mohr stress diagram. Also shown is the resulting failure envelope for a cohesive–brittle–frictional (CBF) model.



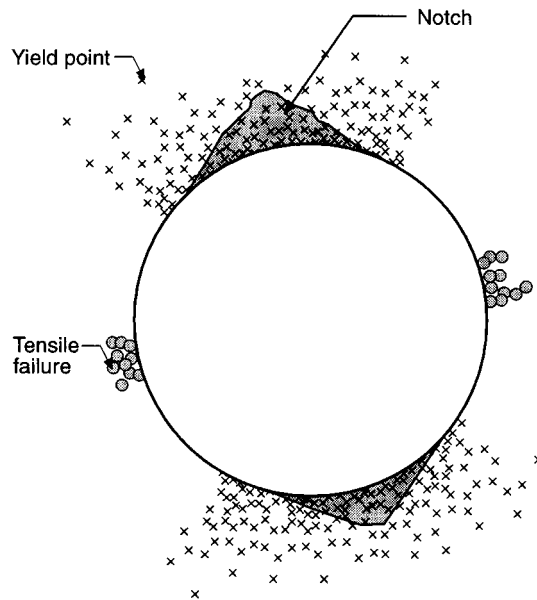
failure. It defines the limit for the initiation of cracking or damage, the first stage in the failure process. It appears that once the process is initiated by removing the confining stress, the final shape of the failed zone around a single opening will not extend beyond the region that was initially damaged, i.e., where cohesion loss has occurred. Recently, Castro et al. (1996) have shown that the constant-deviatoric-stress criterion can also be used to predict the extent of brittle failure around underground openings in moderately jointed rock masses.

Summary

Although the numerical analyses described in this section were only two-dimensional, it is immediately obvious that predicting the depth and extent of stress-induced progressive brittle failure in a homogeneous rock mass is a challenging task. These numerical studies suggest that continuum models using either iterative slab-removal schemes or strain-softening models using conventional frictional failure criterion do not adequately predict the extent of damage measured around the test tunnel. As stated previously, the major hurdle for the continuum models is the tracking of the failure process from crack initiation through to slabbing and spalling.

Back-analyses, although necessary to establish the rock mass strength on the boundary of the tunnel, can be misleading, as this approach implies that the rock mass strength, everywhere around the tunnel, is equivalent to the back-calculated

Fig. 56. Damage, predicted by the numerical program PHASES, around the Mine-by test tunnel using the cohesive–brittle–frictional constitutive model.



strength. As shown by the microseismic studies, the damage, i.e., the number of microseismic events, decreases radially away from the tunnel wall. Hence the back-calculated strength is only applicable to the tunnel perimeter and cannot be used for the general strength of the rock mass.

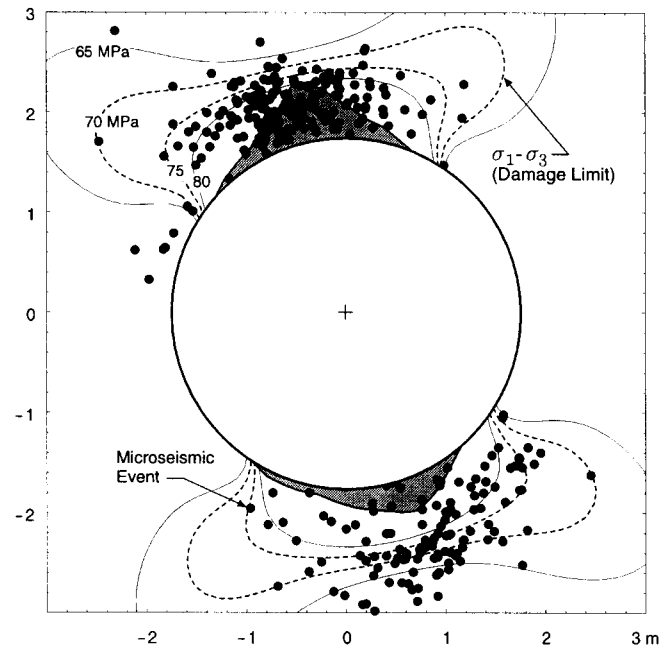
The simple constant-deviatoric-stress criterion appears to be the most promising approach in estimating the depth of brittle failure. This criterion simply indicates the maximum depth of damage and there is no evidence at present, from the studies carried out for the Mine-by Experiment, to suggest that the slabbing process extends beyond this damage limit. The application of the criterion by Castro et al. (1996) to jointed rocks also supports this notion. The constant-deviatoric-stress criterion captures a fundamental characteristic of brittle failure, the initiation of the loss of cohesion. The introduction of the cohesive–brittle–frictional model, which includes the essential elements of the brittle-failure process, may provide a more realistic estimate of stresses in the rock mass around the notch, compared with the elastic analyses. From this perspective, this approach may be more useful in designing support systems.

Conclusions

The progressive failure of Lac du Bonnet granite was investigated by damage-controlled testing and related to the Griffith locus. The test results show that as Lac du Bonnet granite is damaged, a portion of its cohesive strength is lost, and friction is mobilized. The loss in cohesion was traced using the Griffith locus. For small amounts of damage, this cohesion loss can amount to 50% or more of the initial cohesion. In the laboratory this damage was accumulated by following a monotonically increasing loading path.

The laboratory physical models testing program revealed that a strength-scale effect is strongly evident for boreholes that are less than 75 mm in diameter and increases with decreasing diameter. However, with boreholes greater than 75 mm in

Fig. 57. Damage limit defined by the constant-deviatoric-stress criterion ($\sigma_1 - \sigma_3$).



diameter the laboratory strength of the rock around the borehole approaches the unconfined compressive strength, σ_c , of the rock. In situ, the boreholes showed only minor strength-scale effects, and the calculated stress at which borehole instability occurred was about $0.60\sigma_c$. The difference between the laboratory results and the in situ results is attributed to the difference in stress path.

The rock mass near the face of an advancing excavation follows a complex stress path. In many situations the maximum stress at a point will increase, unload, and subsequently increase again as the tunnel advances towards the point and passes it, while at the same time the confining stress decreases. The stress path near the tunnel face cannot be duplicated in the laboratory at any reasonable scale because, in addition to the change in stress magnitude near the face, the principal stress directions are also changing.

In the studies carried out at URL, the failure process around the underground excavations begins at low confining stresses when the deviatoric stresses exceed the in situ crack-initiation stress, which for Lac du Bonnet granite is about 70–75 MPa. Once this threshold is crossed, the path to failure will dictate the ultimate strength of the rock. In the laboratory, where the loads monotonically increase, the short-term unconfined compressive rock strength is about 225 MPa. However, in situ, the damage resulting from the loading path reduces the in situ strength on the boundary of the tunnel to between 100 and 120 MPa or about $0.5\sigma_c$. The amount of damage the loading path creates will be highest at the surface of the opening where confinement is zero and stress concentrations are greatest, and will decrease with increasing distance into the rock. The distribution of damage is a key contributing factor controlling the depth of failure in brittle rock.

The cracking that occurs at the tunnel face, prior to the development of the notch, appears to define the extent and shape of the failure region, i.e., where the notch develops.

Hence, it is unreasonable to expect two-dimensional analyses to accurately capture this three-dimensional process. Traditional frictional-failure criterion significantly underpredicted the depth of failure around the test tunnel. However, the constant-deviatoric-stress criterion given by $\sigma_1 - \sigma_3 = \frac{1}{3} \sigma_c$ was found to provide an adequate estimate of the radial extent of the failure, using simple two-dimensional elastic plane-strain analyses. Although it is recognized that this criterion is somewhat conservative, it does provide a simple means for estimating the depth of failure. The fundamental assumption in the constant-deviatoric-stress criterion is that at low confining stresses, such as those which occur around underground openings, the brittle-failure process is dominated by cohesion loss. It must be realized that this failure criterion may only be applicable for the near-field rock mass around underground openings and may not be appropriate for estimating the far-field rock mass strength.

Acknowledgements

It is indeed an honour to present the 1993 Canadian Geotechnical Colloquium and I wish to express my sincere appreciation to the Canadian Geotechnical Society. The work presented in this colloquium was a team effort and I would like to acknowledge and thank the many people who have contributed directly and indirectly: first, Prof. Norbert Morgenstern, who gave me an opportunity to learn the foundations of geotechnical engineering; Profs. Brian Stimpson and Emery Lajtai at the University of Manitoba for introducing me to cracks and fracture mechanics; Profs. Peter Kaiser and Dougal McCreath of Laurentian University for stimulating discussion on rock failure processes; the Mine-by Experiment Committee; my friends and colleagues at the Underground Research Laboratory, Drs. Neil Chandler, Rodney Read, and Edward Dzik, and Mr. Jason Martino; and finally AECL, in particular Mr. Gary Simmons. This work was supported by the Canadian Nuclear Fuel Waste Management Program, which is jointly funded by AECL and Ontario Hydro under the auspices of the CANDU Owners Group, and by the Natural Sciences and Engineering Research Council of Canada.

References

- Aki, K., and Richards, P. 1980. Quantitative seismology: theory and methods. W.H. Freeman, San Francisco.
- Bieniawski, Z.T. 1967. Mechanism of brittle fracture of rock, Parts I, II and III. *International Journal of Rock Mechanics and Mining Sciences and Geomechanics Abstracts*, 4(4): 395–430.
- Bieniawski, Z.T. 1979. The geomechanics classification in rock engineering applications. *In Proceedings, 4th International Society of Rock Mechanics Congress, Montreux*. Vol. 2. A.A. Balkema, Rotterdam, pp. 41–48.
- Brace, W.F., Paulding, B., and Scholz, C. 1966. Dilatancy in the fracture of crystalline rocks. *Journal of Geophysical Research*, 71: 3939–3953.
- Brown, E.T. (Editor). 1981. Rock characterization testing and monitoring, ISRM suggested methods. Pergamon Press, Oxford.
- Carter, B.J. 1992. Size and stress gradients effects on fracture around cavities. *Rock Mechanics and Rock Engineering*, 25(3): 167–186.
- Carvalho, J.L., Hoek, E., and Corkum, B.T. 1991. PHASES—a 2D hybrid finite/boundary element program for calculating stresses and estimating support around underground openings, version 2. Rock Engineering Group, University of Toronto, Toronto, Ont.
- Castro, L.A.M., McCreath, D.R., and Oliver, P. 1996. Rockmass damage initiation around the Sudbury Neutrino Observatory cavern. *In Proceedings, 2nd North American Rock Mechanics Symposium, Montréal*. Vol. 2. Edited by M. Aubertin, F. Hassani, and H. Mitri. A.A. Balkema, Rotterdam, pp. 1589–1595.
- Collins, D.S., and Young, R.P. 1992. Monitoring and source location of microseismicity induced by excavation of the Mine-by Test Tunnel: preliminary analysis. Atomic Energy of Canada Ltd. Report RP013AECL, Engineering Seismology Laboratory, Queen's University, Kingston, Ont.
- Collins, D.S., Baker, C., and Young, R.P. 1994. Source parameters of excavation-induced seismicity from the Mine-by tunnel. Atomic Energy of Canada Ltd. Report RP028AECL, Applied Seismology and Rock Physics Laboratory, Keele University, Staffordshire, U.K.
- Cook, N.G.W. 1965. The failure of rock. *International Journal of Rock Mechanics and Mining Sciences and Geomechanics Abstracts*, 2: 389–403.
- Cundall, P.A., and Board, 1988. A microcomputer program for modelling large-strain plasticity problems. *In Proceedings, 6th International Conference on Numerical Methods in Geomechanics, Innsbruck, Austria*. Edited by G. Swoboda. A. A. Balkema, Rotterdam, pp. 2101–2108.
- Cundall, P.A., Potyondy, D.O., and Lee, C.A. 1996. Micromechanics-based models for fracture and breakout around the Mine-by tunnel. *In Proceedings, International Conference on Deep Geological Disposal of Radioactive Waste, Winnipeg*. Edited by J.B. Martino and C.D. Martin. Canadian Nuclear Society, Toronto, pp. 113–122.
- Curran, J.H., and Corkum, B.T. 1995a. Examine^{2D}—a 2D boundary element program for calculating stresses around underground excavations in rock, version 5. Rock Engineering Group, University of Toronto, Toronto, Ont.
- Curran, J.H., and Corkum, B.T. 1995b. Examine^{3D}—a 3D boundary element program for calculating stresses around underground excavations in rock. Rock Engineering Group, University of Toronto, Toronto, Ont.
- Everitt, R.A., Brown, A., Davison, C.C., Gascoyne, M., and Martin, C.D. 1990. Regional and local setting of the Underground Research Laboratory. *In Proceedings, International Symposium on Unique Underground Structures, Denver*. Vol. 2. Edited by R. S. Sinha. CSM Press, Denver, Colo., pp. 1–23.
- Ewy, R.T., and Cook, N.G.W. 1990. Deformation and fracture around cylindrical openings in rock, Parts I and II. *International Journal of Rock Mechanics and Mining Sciences and Geomechanics Abstracts*, 27: 387–427.
- Gramberg, J. 1989. A non-conventional view on rock mechanics and fracture mechanics. A.A. Balkema, Rotterdam.
- Griffith, A.A. 1921. The phenomena of rupture and flow in solids. *Philosophical Transactions of the Royal Society of London, Series A*, 221: 163–198.
- Haimson, B.C., and Herrick, C.G. 1989. Borehole breakouts and *in situ* stress. *In Proceedings, 12th Annual Energy-Sources Technology Conference and Exhibition, Drilling Symposium*. American Society of Mechanical Engineers, New York, pp. 17–22.
- Hoek, E. 1965. Rock fracture under static stress conditions. CSIR Report MEG 383, National Mechanical Engineering Research Institute, Council for Scientific and Industrial Research, Pretoria, South Africa.
- Hoek, E., and Brown, E.T. 1980a. Empirical strength criteria for rock masses. *ASCE Journal of the Geotechnical Engineering Division*, 106(GT9): 1013–1035.
- Hoek, E., and Brown, E.T. 1980b. Underground excavations in rock. The Institution of Mining and Metallurgy, London.
- Hoek, E., and Brown, E.T. 1988. The Hoek–Brown failure criterion—a 1988 update. *In Proceedings, 15th Canadian Rock Mechanics Symposium, Toronto*. Edited by J. H. Curran. Department of Civil Engineering, University of Toronto, Toronto, Ont., pp. 31–38.

- Hoek, E., Kaiser, P.K., and Bawden, W.F. 1995. Support of underground excavations in hard rock. A. A. Balkema, Rotterdam.
- Holcomb, D.J., and Martin, R.J. 1985. Determining peak stress history using acoustic emissions. *In Proceedings, 26th U.S. Symposium on Rock Mechanics, Rapid City. Vol. 1. Edited by E. Ashworth.* A.A. Balkema, Rotterdam, pp. 715–722.
- Hudson, J.A., Brown, E.T., and Fairhurst, C. 1972. Shape of the complete stress-strain curve for rock. *In Proceedings, 13th U.S. Symposium on Rock Mechanics, Urbana. Edited by E. Cording.* American Society of Civil Engineers, New York, pp. 773–795.
- Jaeger, J.C., and Cook, N.G.W. 1979. *Fundamentals of rock mechanics.* 3rd ed. Chapman and Hall, London.
- Kaiser, P.K. 1994. Observational modelling approach for design of underground openings. *In Proceedings, International Society for Rock Mechanics, South African National Group, The Application of Numerical Modelling in Geotechnical Engineering, Pretoria,* pp. 1–8.
- Kemeny, J.M., and Cook, N.G.W. 1986. Effective moduli, nonlinear deformation and strength of a cracked elastic solid. *International Journal of Rock Mechanics and Mining Sciences and Geomechanics Abstracts, 23(2):* 107–118.
- Kemeny, J.M., and Cook, N.G.W. 1991. Micromechanics of deformation in rocks. *In Toughening mechanics in quasi-brittle materials. Vol. 2. Edited by S P. Shaw.* Kluwer Academic Publishers Group, Dordrecht, The Netherlands, pp. 155–188.
- Lajtai, E.Z. 1972. Effect of tensile stress gradient on brittle fracture initiation. *International Journal of Rock Mechanics and Mining Sciences and Geomechanics Abstracts, 9:* 569–578.
- Lajtai, E.Z., Carter, B.J., and Duncan, E.J.S. 1991. Mapping the state of fracture around cavities. *Engineering Geology, 31:* 277–289.
- Lee, M.Y., and Haimson, B.C. 1993. Laboratory study of borehole breakouts in Lac du Bonnet granite: a case of extensile failure mechanism. *International Journal of Rock Mechanics and Mining Sciences and Geomechanics Abstracts, 30(7):* 1039–1045.
- Lockner, D.A., Byerlee, J.D., Kuksenko, V., Ponomarev, A., and Sidorin, A. 1992. Observations of quasistatic fault growth from acoustic emissions. *In Fault mechanics and transport properties of rocks. Edited by B. Evans and T.-f. Wong.* Academic Press, London, pp. 3–31.
- Martin, C.D. 1990. Characterizing *in situ* stress domains at the AECL Underground Research Laboratory. *Canadian Geotechnical Journal, 27:* 631–646.
- Martin, C.D. 1993. Strength of massive Lac du Bonnet granite around underground openings. Ph.D. thesis, Department of Civil and Geological Engineering, University of Manitoba, Winnipeg, Man.
- Martin, C.D., and Chandler, N.A. 1993. Stress heterogeneity and geological structures. *International Journal of Rock Mechanics and Mining Sciences and Geomechanics Abstracts, 30(7):* 993–999.
- Martin, C.D., and Chandler, N.A. 1994. The progressive fracture of Lac du Bonnet granite. *International Journal of Rock Mechanics and Mining Sciences and Geomechanics Abstracts, 31(6):* 643–659.
- Martin, C.D., and Kaiser, P.K. 1996. Mine-by Experiment Committee report, Phase 1: excavation response, summary and implications. Atomic Energy of Canada Limited, Report AECL–11382. Available from SDDO, AECL Research, Chalk River, Ont.
- Martin, C.D., and Stimpson, B. 1994. The effect of sample disturbance on laboratory properties of Lac du Bonnet granite. *Canadian Geotechnical Journal, 31(5):* 692–702.
- Martin, C.D., Martino, J.B., and Dzik, E.J. 1994. Comparison of borehole breakouts from laboratory and field tests. *In Proceedings, EUROCK'94, SPE/ISRM Rock Mechanics in Petroleum Engineering, Delft.* A.A. Balkema, Rotterdam, pp. 183–190.
- Martin, C.D., Young, R.P., and Collins, D.S. 1995. Monitoring progressive failure around a tunnel in massive granite. *In Proceedings, 8th ISRM Congress on Rock Mechanics, Tokyo. Vol. 2. Edited by T. Fujii.* A.A. Balkema, Rotterdam, pp. 627–633.
- Martin, C.D., Read, R.S., and Martino, J.B. 1997. Observations of brittle failure around a circular test tunnel. *International Journal of Rock Mechanics and Mining Sciences & Geomechanical Abstracts, 34.*
- Mastin, L. 1984. The development of borehole breakouts in sandstone. M. Sc. thesis, Stanford University, Berkeley, Calif.
- McGarr, A. 1994. Some comparisons between mining-induced and laboratory earthquakes. *Pure and Applied Geophysics, 142(3/4):* 467–489.
- Myrvang, A.M. 1991. Estimation of *in situ* compressive strength of rocks from *in situ* stress measurements in highly stressed rock structures. *In Proceedings, 7th ISRM Congress on Rock Mechanics, Aachen. Edited by W. Wittke.* A.A. Balkema, Rotterdam, pp. 573–575.
- Onagi, D.P., Keith, S.G., and Kuzyk, G.W. 1992. Non-explosive excavation technique developed for the excavation of AECL's Mine-by Experiment Test Tunnel at the Underground Research Laboratory. *In Proceedings, 10th TAC Annual Canadian Tunneling Conference, Banff.* Bi-Tech Publishers, Vancouver, B.C., pp. 1–11.
- Orowan, E. 1949. Fracture and strength of solids. *Reports on Progress in Physics, 12:* 185–232.
- Pelli, F., Kaiser, P.K., and Morgenstern, N.R. 1991. An interpretation of ground movements recorded during construction of the Donkin-Morien tunnel. *Canadian Geotechnical Journal, 28(2):* 239–254.
- Pestman, B.J., and Van Munster, J.G. 1996. An acoustic emission study of damage development and stress-memory effects in sandstone. *International Journal of Rock Mechanics and Mining Sciences and Geomechanics Abstracts, 33(6):* 585–593.
- Read, R.S. 1994. Interpreting excavation-induced displacements around a tunnel in highly stressed granite. Ph.D. thesis, Department of Civil and Geological Engineering, University of Manitoba, Winnipeg, Man.
- Read, R.S., and Martin, C.D. 1992. Monitoring the excavation-induced response of granite. *In Proceedings, 33rd U.S. Symposium on Rock Mechanics, Santa Fe. Edited by J. Tillerson and W. Wawersik.* A.A. Balkema, Rotterdam, pp. 201–210.
- Read, R.S., and Martin, C.D. 1996. Technical summary of AECL's Mine-by Experiment Phase 1: excavation response. Atomic Energy of Canada Limited, Report AECL–11311. Available from SDDO, AECL Research, Chalk River, Ont.
- Read, R.S., Martin, C.D., and Dzik, E.J. 1995. Asymmetric borehole breakouts at the url. *In Proceedings, 35th U.S. Symposium on Rock Mechanics, Lake Tahoe. Edited by J. Daemen and R. Schultz.* A.A. Balkema, Rotterdam, pp. 879–884.
- Schmertmann, J.H., and Osterberg, J.O. 1960. An experimental study of the development of cohesion and friction with axial strain in saturated cohesive soils. *In Research Conference on Shear Strength of Cohesive Soils, Boulder, Colo.* American Society of Civil Engineers, New York, pp. 643–694.
- Schmidtke, R.H., and Lajtai, E. 1985. The long-term strength of Lac du Bonnet granite. *International Journal of Rock Mechanics and Mining Sciences and Geomechanics Abstracts, 22(6):* 461–465.
- Scholz, C.H. 1968. Microfracturing and the inelastic deformation of rock in compression. *Journal of Geophysical Research, 73(4):* 1417–1432.
- Stacey, T.R. 1981. A simple extension strain criterion for fracture of brittle rock. *International Journal of Rock Mechanics and Mining Sciences and Geomechanics Abstracts, 18:* 469–474.
- Starr, A.T. 1928. Slip in a crystal and rupture in a solid due to shear. *Proceedings of the Cambridge Philosophical Society, 24:* 489–500.
- Talebi, S., and Young, R.P. 1992. Microseismic monitoring in highly stressed granite: relation between shaftwall cracking and *in situ* stress. *International Journal of Rock Mechanics and Mining Sciences and Geomechanics Abstracts, 29(1):* 25–34.
- Tapponnier, P., and Brace, W.F. 1976. Development of stress-induced microcracks in Westerly granite. *International Journal of Rock*

- Mechanics and Mining Sciences and Geomechanics Abstracts, **13**: 103–112.
- Wawersik, W.R., and Brace, W.F. 1971. Post failure behaviour of a granite and diabase. *Rock Mechanics and Rock Engineering*, **3**: 61–85.
- Wu, H., and Pollard, D.D. 1995. Possible secondary fracture patterns due to a change in the direction of loading. *In Proceedings, Conference on Fractured and Jointed Rock Masses, Lake Tahoe, June 1992. Edited by L.R. Myer, C.-F. Tsang, N.G.W. Cook, and R.E. Goodman.* A.A. Balkema, Rotterdam, pp. 487–493.
- Zheng, Z., Kemeny, J., and Cook, N.G.W. 1989. Analysis of borehole breakouts. *Journal of Geophysical Research*, **94**(B6): 7171–7182.